Computer Methods in Applied Mechanics and Engineering 199 (2010) 1992–2013

Contents lists available at ScienceDirect

Computer Methods in Applied Mechanics and Engineering

journal homepage: www.elsevier.com/locate/cma

Asynchronous multi-domain variational integrators for nonlinear hyperelastic solids

Michal Beneš [b], Karel Matouš [a,*,1]

[a] Department of Aerospace and Mechanical Engineering, University of Notre Dame, Notre Dame, IN 46556, USA
[b] Computational Science and Engineering, University of Illinois at Urbana-Champaign, Urbana, IL 61801, USA

ARTICLE INFO

Article history:
Received 11 March 2009
Received in revised form 5 January 2010
Accepted 24 February 2010
Available online 11 March 2010

Keywords:
Initial/boundary-value problem
Asynchronous variational integrators
Domain decomposition
Nonlinear stability/conservation analysis
Hyperelasticity

ABSTRACT

We present the asynchronous multi-domain variational time integrators with a dual domain decomposition method for the initial hyperbolic boundary-value problem in hyperelasticity. Variational time integration schemes, based on the principle of minimal action within the Lagrangian framework, are constructed for the equation of motion and implemented into a variational finite element framework, which is systematically derived from the three-field de Veubeke-Hu-Washizu variational principle to accommodate the incompressibility constraint present in an analysis of nearly-incompressible materials. For efficient parallel computing, we use the dual domain decomposition method with local Lagrange multipliers to ensure the continuity of the displacement field at the interface between subdomains. The α-method for time discretization and the multi-domain spatial decomposition enable us to use different types of integrators (explicit vs. implicit) and different time steps on different parts of a computational domain, and thus efficiently capture the underlying physics with less computational effort. The energy conservation of our nonlinear, midpoint, asynchronous integration scheme is investigated using the Energy method, and both local and the global energy error estimates are derived. We illustrate the performance of proposed variational multi-domain time integrators by means of three examples. First, the method of manufactured solutions is used to examine the consistency of the formulation. In the second example, we investigate energy conservation and stability. Finally, we apply the method to the motion of a heterogeneous plane domain, where different integrators and time discretization steps are used accordingly with disparate material data of individual parts.

1. Introduction

In time-dependent scientific simulations, where different multi-physics solvers are often coupled, the time integrator is an important component. Typically, the partial differential equations (PDEs) are solved by discretizing the domain spatially using finite elements or finite volumes, then integrating over time using a numerical ordinary differential equation (ODE) solver. Both the coupling between domains and the time integration must be handled with care to avoid numerical instability, since the stability and accuracy of such coupling are dictated not only by the individual local time step limits, but also by the data transfer method across the interface. Moreover, the stability and accuracy requirements for different domains may necessitate different time steps. For example, a stiff material domain may require small time steps for numerical stability, or a fluid domain may require small time steps to resolve boundary layers accurately, while other material domains may permit a larger time step.

Another challenge when solving these problems is in the spatial discretization, allowing the ability to link domains with non-matching discretizations. Due to their size, these simulations often require parallel computing, which can be effectively done using domain decomposition. For elliptic problems, Farhat and Roux [16] proposed the popular FETI method, which was subsequently extended to transient problems [14]. It enforces continuity between domains by adding an additional constraint with Lagrange multipliers. Park et al. [36] developed a variant using local Lagrange multipliers that constrains domains to an intermediate interface rather than directly to each other. Such an intermediate interface is used in Park et al. [37] and Brezzi and Marini [9] to handle domains with non-matching meshes, as illustrated in Fig. 1.

To achieve an efficient, stable, and accurate integrator, several issues must be addressed. For accurate long time integration, it is desirable that the integrator conserves energy and preserves momentum. It is well known, that ODE integrators that discretize

* Corresponding author. Department of Aerospace and Mechanical Engineering, University of Notre Dame, 367 Fitzpatrick Hall of Engineering, Notre Dame, IN 46556-5637, USA. Tel.: +1 574 631 1376.
E-mail address: kmatous@nd.edu (K. Matouš).
URL: http://www.nd.edu/~kmatous (K. Matouš).
[1] U.S. Department of Energy, B523819.

0045-7825/$ – see front matter © 2010 Elsevier B.V. All rights reserved.
doi:10.1016/j.cma.2010.02.017

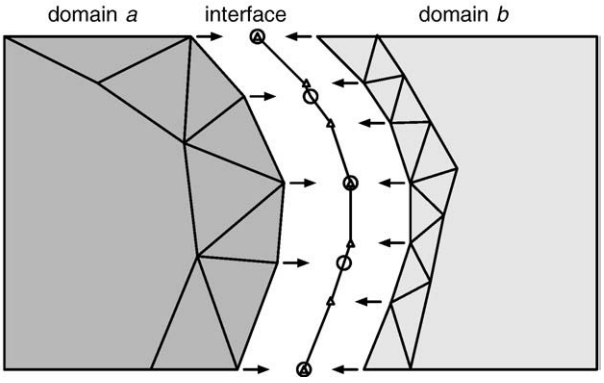

Fig. 1. Domain decomposition with a common interface between domains. Arrows represent the local Lagrange multipliers constraining each domain to the interface.

the differential equation itself, such as Runge-Kutta methods, often artificially dissipate energy to achieve numerical stability. To relax the time step constraint imposed by stability requirements, mixed methods or multi-time methods with different time steps for each domain were proposed. Belytschko and Mullen [6,7] were the first to use a mixed explicit–implicit method with a nodal partition, while Hughes and Liu [26,27] introduced a mixed method using an element partition. Belytschko et al. [8] introduced subcycling for first-order problems, and later extended it to non-integer time step ratios [5]. Neal and Belytschko [33] developed subcycling with non-integer ratios for second-order structural problems. Although popular, the stability of second-order subcycling methods has been elusive. Smolinski and Sleith [40] contrived an explicit subcycling algorithm for second-order problems that was proved stable [41], but is less accurate than other algorithms. Daniel [11] showed that Neal and Belytschko's algorithm is "statistically stable", but unstable for certain time steps smaller than the expected stability limit. More recently, Combescure and Gravouil [10,21] developed a FETI-like transient method that enforces continuity of velocities and is proved stable but dissipative for subcycling. Prakash and Hjelmstad [38] improved this method to be stable and non-dissipative for subcycling, but their method is based on binary trees for parallelism and additive operator split, rendering it less popular for nonlinear problems and high-performance computing.

Another set of integrators proposed in recent years are the Variational Integrators. These are derived by discretizing the Lagrangian and applying variational calculus, resulting in methods that preserve momentum, do not dissipate energy and are symplectic. As a result they are superior for long time integration. Variational integrators have been developed by Veselov [42], Wendlandt and Marsden [43], and Marsden and West [31], among others. Kane et al. [29] showed that the popular Newmark method [34] can also be derived variationally. Lew et al. [30] developed an asynchronous variational integrator (AVI) and presented its explicit implementation, where each element has its own time step. The parallel implementation of AVI was presented in Kale and Lew [28].

Time integrators for nonlinear problems and their stability have also generated a high degree of interest. Especially, the energy-controlling or conserving methods have been investigated [19,20,22]. Time integration schemes that conserve the momenta and dissipate the energy in order to diminish unresolved high frequency modes, while maintaining good accuracy were delineated in [3]. Recently, energy-dissipative momentum-conserving time stepping algorithms for finite strain multiplicative plasticity were presented by Armero [2].

Based on the promising results of the variational integrators and their deep mathematical structure, in Section 3 we present a method for integrating nonlinear problems with domain decomposition. In particular, we build on our previous work focused on ODEs [18] and extend it to PDEs for nearly-incompressible materials. Quasi-incompressible material behavior is treated by a three-field de Veubeke-Hu-Washizu variational principle [19,32,39]. Note that modeling of nearly-incompressible materials is challenging, especially for explicit integrators, since the wave speed $\to\infty$ as $\nu\to 1/2$, and thus $\Delta t\to 0$. We develop an asynchronous integrator that allows each domain to use its own arbitrary time step and integrator. We use a variational approach based on the generalized α-method to take advantage of its favorable properties and enforce the continuity of displacements with a common interface. The constraint is applied by using local Lagrange multipliers in context of the dual domain decomposition method. Displacement constraints avoid discontinuities between domains in the cases where continuity of velocities is only enforced.

In Section 4, we present the energy conservation analysis of our integrators for both the synchronous and asynchronous time stepping using the midpoint rule, $\alpha=1/2$. We follow the approach by Hauret and Le Tallec [22]. By treating the constraints variationally, we ensure stability in domain coupling. The synchronous implicit midpoint version achieves a conditional stability with $\mathcal{O}(\Delta t^3)$, while with asynchronous steps it is conditionally stable with a local criterion $\mathcal{O}((\Delta t^k)^2)$. However, we show that for our common interface, the global energy control still holds with $\mathcal{O}(\Delta t^3)$. Our method accommodates nonlinear problems very naturally and the high degree of parallelism is preserved. Note that rigorous nonlinear stability analysis is not part of this investigation. For linear stability analysis of AVI, we point the interested reader to the work of Fong et al. [17].

We present examples in Section 5 involving the convergence study, energy conservation study, and the mixed implicit/explicit integration test that demonstrates the potential of the method for error control. Finally, several conclusions are made in Section 6.

The main contributions of the present work are: *i)* Combination of the most recent advances in asynchronous multi-domain variational time integrators with a dual domain decomposition method in the context of a mixed three-field de Veubeke-Hu-Washizu variational principle for nearly-incompressible solids. *ii)* Introduction of a linearly interpolated common interface and the local Lagrange multiples in the space/time domain that allow for mixed, asynchronous implicit/explicit integration amenable to parallel computation. *iii)* The energy conservation analysis of the midpoint integrator by the Energy method. *iv)* Unique examples, based on the Method of Manufactured Solutions, that provide a rigorous verification testbeds.

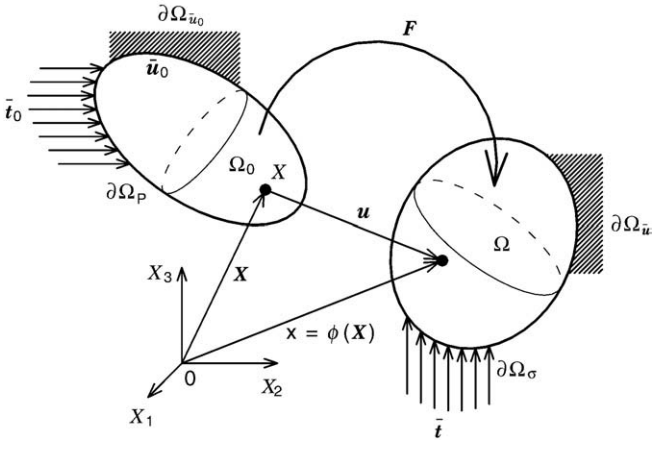

Fig. 2. Problem description.

2. Governing equations — continuum problem

Let the open set $\Omega_0 \subset \mathbb{R}^3$ be the reference configuration of a given (compressible or nearly-incompressible) body at time t_0. Each point X is associated by a bijective map with its position in that configuration: $X \rightarrow \mathbf{X} \in \Omega_0$, as shown in Fig. 2.

In the absence of displacement discontinuities, a unique differentiable deformation map $\phi: \Omega_0 \times [0, T] \rightarrow \mathbb{R}^3$ describing a motion exists, such that any displaced position at a current time $t \in [0, T]$, where $[0, T] \subset \mathbb{R}^+$ denotes the time of interest, is determined as $\boldsymbol{x} = \phi(\boldsymbol{X}, t)$ with the difference being the displacement field $\boldsymbol{u}(X, t) = \boldsymbol{x} - \boldsymbol{X}$. The deformation gradient $\boldsymbol{F}(\boldsymbol{X}, t)$ is obtained by taking the gradient of the deformation map $\boldsymbol{F} = \nabla_0 \phi$, where ∇_0 is the gradient with respect to $\boldsymbol{X}$, and the Jacobian of the deformation map is given by $J(\boldsymbol{X}, t) = det\, \boldsymbol{F}$. We also define the right Cauchy-Green deformation tensor $\boldsymbol{C}(\boldsymbol{X}, t) = \boldsymbol{F}^T \boldsymbol{F}$.

The initial/boundary-value problem of motion reads

$$\begin{aligned}
\rho_0 \frac{\partial^2 \boldsymbol{u}}{\partial t^2} &= \nabla_0 \cdot \mathbf{P} + \mathbf{f}_0 && \text{in } \Omega_0 \times (0, T), \\
\boldsymbol{u} &= \overline{\boldsymbol{u}}_0 && \text{on } \partial\Omega \overline{u} \times (0, T), \\
\boldsymbol{P} \cdot \boldsymbol{N}_0 &= \bar{\mathrm{t}}_0 && \text{on } \partial\Omega_P \times (0, T), \\
\boldsymbol{u}(\mathbf{X}, 0) &= \boldsymbol{u}_0 && \text{in } \Omega_0, \\
\frac{\partial \boldsymbol{u}}{\partial t}(\mathbf{X}, 0) &= \dot{\boldsymbol{u}}_0 && \text{in } \Omega_0,
\end{aligned} \tag{1}$$

where $\rho_0(\boldsymbol{X}, t) = J\rho$ represents the reference mass density and $\rho = \rho(\boldsymbol{X}, t)$ is the deformed mass density, $\boldsymbol{P} = \boldsymbol{P}(\boldsymbol{X}, \boldsymbol{F}(\boldsymbol{X}, t))$ is the first Piola-Kirchhoff stress, $\boldsymbol{f}_0 = \boldsymbol{f}_0(\boldsymbol{X}, t)$ denotes the external body force, $\overline{\boldsymbol{u}}_0 = \overline{\boldsymbol{u}}_0(X, t)$ is the prescribed displacement on the boundary $\partial\Omega_{\overline{u}}$, $\overline{t}_0 = \overline{t}_0(\boldsymbol{X}, t)$ represents the known surface load on the boundary $\partial\Omega_P$ and N_0 represents the unit normal to $\partial\Omega_P$. Here $\frac{\partial \boldsymbol{u}}{\partial t}(\mathbf{X}, t)$ denotes the material velocity $\dot{\boldsymbol{u}}(\boldsymbol{X}, t)$ and $\frac{\partial^2 \boldsymbol{u}}{\partial t^2}$ represents the material acceleration $\ddot{\boldsymbol{u}}(\mathbf{X}, t)$, respectively. To render the initial/boundary-value problem well posed, initial conditions $\mathbf{u}_0$ and $\dot{\mathbf{u}}_0$ are given for both displacement $\boldsymbol{u}$ and velocity $\dot{\boldsymbol{u}}$. Note that $\partial\Omega_{\overline{\boldsymbol{u}}_0}$ and $\partial\Omega_P$ are smooth open disjoint subsets of $\partial\Omega_0$ such that $\partial\Omega_0 = \partial\Omega_{\overline{\boldsymbol{u}}_0} \cup \partial\Omega_P$ and the 1-dimensional measure of $\partial\Omega_0 - (\partial\Omega_{\overline{\boldsymbol{u}}_0} \cup \partial\Omega_P)$ is zero.

2.1. A three-field continuous Lagrangian framework

In this work, we are interested in variational integrators within the domain decomposition framework to solve the equation of motion, Eq. (1), in the context of nearly-incompressible material behavior, which requires a special numerical treatment. For clarity and completeness of the presentation, we start with a continuous variational formulation. The derivation of variational integrators for computing the motion in the discrete setting will follow analogously. To account properly for a nearly-incompressible material response, we employ a three-field de Veubeke-Hu-Washizu variational principle [19,32,39].

In general, the volume-preserving part of a deformation gradient reads

$$\hat{\boldsymbol{F}}(\boldsymbol{X}, t) = J^{-\frac{1}{3}} \boldsymbol{F}, \tag{2}$$

and the volumetric term $\theta(\mathbf{X}, t)$ is given by

$$\theta = J. \tag{3}$$

Next, we introduce a mixed deformation gradient $\overline{\boldsymbol{F}}(\boldsymbol{X}, t) = \theta^{\frac{1}{3}} \hat{\boldsymbol{F}}$, such that an additional variable θ now represents a mixed Jacobian ($\theta \equiv \det(\overline{\mathrm{F}})$). In the finite element formulation, introduced hereafter, Eq. (3) is satisfied in a weak sense.

A mixed variational formulation, in the Lagrangian frame, is governed by a *Lagrangian* defined as the kinetic minus the potential energy

$$L(\boldsymbol{u}, \dot{\boldsymbol{u}}, \theta, p) = T(\dot{\boldsymbol{u}}) - V(\boldsymbol{u}, \theta, p), \tag{4}$$

where

$$T(\dot{\boldsymbol{u}}) = \frac{1}{2} \int_{\Omega_0} \rho_0 \frac{\partial \boldsymbol{u}}{\partial t} \cdot \frac{\partial \boldsymbol{u}}{\partial t} \mathrm{d}\Omega_0, \tag{5}$$

and

$$V(\boldsymbol{u}, \theta, p) = \underbrace{\int_{\Omega_0} W\left(\widehat{\boldsymbol{C}}, \theta\right) \mathrm{d}\Omega_0 + \int_{\Omega_0} p(J - \theta) \mathrm{d}\Omega_0}_{E_{in}} - \underbrace{\left(\int_{\Omega_0} \boldsymbol{f}_0 \cdot \boldsymbol{u} \mathrm{d}\Omega_0 + \int_{\partial\Omega_P} \bar{\boldsymbol{t}}_0 \cdot \boldsymbol{u} \mathrm{d}S_0 \right)}_{E_{ex}} \tag{6}$$

with E_{in} being defined as the internal and E_{ex} representing the external energy, respectively. The total energy E of the system is simply $E = T + V$.

As is typical for mixed methods [4,39], the stored energy function $W(\hat{\boldsymbol{C}}, \theta)$ is additively decomposed into distortional $\hat{W}$ and dilatational U parts

$$W(\widehat{\boldsymbol{C}},\theta) = \widehat{W}(\boldsymbol{C}) + U(\theta), \tag{7}$$

with $\widehat{\boldsymbol{C}}(\mathbf{X},t) = J^{-\frac{2}{3}}\boldsymbol{C}$ being the isochoric part of the right Cauchy-Green tensor. A traditional nearly-incompressible neo-Hookean potential $\widehat{W}(\boldsymbol{C}) = \frac{1}{2}\mu\left(\mathrm{tr}\,\widehat{\boldsymbol{C}}-3\right)$ and a simple volumetric function $U(\theta) = \frac{1}{2}\kappa(\theta-1)^2$ are used in this work, where μ is the shear modulus and κ denotes the bulk modulus, respectively. The hyperelastic constitutive equation yields

$$\boldsymbol{P} = \frac{\partial\hat{W}(\boldsymbol{F})}{\partial\boldsymbol{F}}\bigg|_{\boldsymbol{F}=\bar{\boldsymbol{F}}} + \underbrace{\frac{\mathrm{d}U}{\mathrm{d}\theta}}_{p}\frac{\partial\theta}{\partial\boldsymbol{F}}\bigg|_{\boldsymbol{F}=\bar{\boldsymbol{F}}}, \tag{8}$$

where $p = p(\mathbf{X}, t)$ (see also Eq. (6)) is the hydrostatic pressure.

Now, we introduce an action integral

$$A = A(\boldsymbol{u},\theta,p) = \int_{t_1}^{t_2} L(\boldsymbol{u},\dot{\boldsymbol{u}},\theta,p)\mathrm{d}t, \tag{9}$$

where t_1, t_2 ($t_1<t_2$) are arbitrary times within $(0, T)$ and apply the Hamilton's principle $\delta A(\boldsymbol{u}, \theta, p) = 0$ to obtain a weak form of the initial/boundary-value problem (1). Find $\boldsymbol{u}(\mathbf{X}, t)\in\mathcal{C}([0, T]; H^{1,2})$, $\theta(\mathbf{X}, t)\in\mathcal{C}([0, T]; L^2(\Omega_0))$ and $p(\mathbf{X}, t)\in\mathcal{C}([0, T]; L^2(\Omega_0))$ such that

$$\begin{aligned}
\mathscr{R}_{\boldsymbol{u}} &= \int_0^T\Bigg\{\int_{\Omega_0}\Big[\rho_0\frac{\partial\boldsymbol{u}}{\partial t}\cdot\frac{\partial\delta\boldsymbol{u}}{\partial t} - \hat{\boldsymbol{S}}' : \left(\boldsymbol{F}^T\nabla_0\delta\boldsymbol{u}\right) - pJ\boldsymbol{C}^{-1} : \left(\boldsymbol{F}^T\nabla_0\delta\boldsymbol{u}\right)\Big]\mathrm{d}\Omega_0 \\
&\quad + \int_{\Omega_0}\boldsymbol{F}_0\cdot\delta\boldsymbol{u}\mathrm{d}\Omega_0 + \int_{\partial\Omega_p}\bar{\boldsymbol{t}}_0\cdot\delta\boldsymbol{u}\mathrm{d}S_0\Bigg\}\mathrm{d}t = 0, \\
\mathscr{R}_\theta &= \int_0^T\Big\{\int_{\Omega_0}[p-\kappa(\theta-1)]\delta\theta\,\mathrm{d}\Omega_0\Big\}\mathrm{d}t = 0, \\
\mathscr{R}_p &= \int_0^T\Big\{\int_{\Omega_0}(J-\theta)\delta p\,\mathrm{d}\Omega_0\Big\}\mathrm{d}t = 0,
\end{aligned} \tag{10}$$

hold for every variation $\delta\boldsymbol{u}\in\mathcal{C}([0, T]; H^{1,2})$, $\delta\theta\in\mathcal{C}([0, T]; L^2(\Omega_0))$ and $\delta p\in\mathcal{C}([0, T]; L^2(\Omega_0))$. $\delta\dot{\boldsymbol{u}}(\boldsymbol{X}, t):[0,T]\to L^2(\Omega_0)^3$ is piecewise continuous in $[0, T]$, $\delta\boldsymbol{u}(\boldsymbol{X}, t) = 0$ on $\partial\Omega_{\bar{\boldsymbol{u}}}\times[0, T]$, $\dot{\boldsymbol{u}}(\boldsymbol{X}, t)\in\mathcal{C}([0, T]; H^{0,2})$ and initial data are given by

$$\boldsymbol{u}(\mathbf{X},0) = \boldsymbol{u}_0, \tag{11}$$

$$\dot{\boldsymbol{u}}(\mathbf{X},0) = \dot{\boldsymbol{u}}_0. \tag{12}$$

Here $\hat{\boldsymbol{S}}'(\mathbf{X},t) = 2\frac{\partial\hat{\boldsymbol{W}}}{\partial\boldsymbol{C}}(\boldsymbol{C})$ is the comzputational deviatoric second Piola-Kirchhoff stress. The Hilbert spaces $H^{1,2}$ and $H^{0,2}$ introduced above represent closures of

$$\mathcal{E}(\Omega_0) = \left\{\boldsymbol{u}\in C^\infty(\overline{\Omega}_0)^3;\ \mathrm{supp}\ \boldsymbol{u}\cap\partial\Omega_{\bar{u}} = \varnothing\right\} \tag{13}$$

in the norm $W^{1,2}(\Omega_0)^3$ and $L^2(\Omega_0)^3$, where $W^{1,2}(\Omega_0)^3$ denotes the Sobolev space of square-integrable functions with weak derivatives up to first order with range in $\mathbb{R}^3$, and $L^2(\Omega_0)^3$ is a typical Lebesgue space.

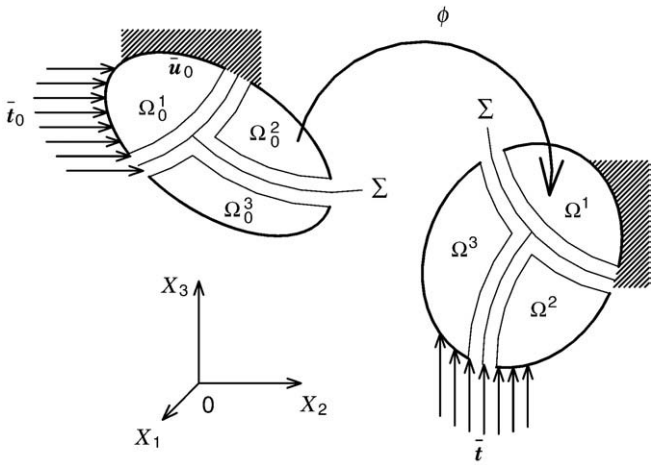

Fig. 3. Domain decomposition. N_D denotes the number of subdomains.

Note that we make no attempt to address issues of existence and uniqueness of the solution. Existence can be proven for certain cases in a suitable Sobolev space [13,25] (typically $\boldsymbol{u}\in W^{1,s}(\Omega_0)^3$, $\dot{\boldsymbol{u}}\in L^2(\Omega_0)^3$ and $p,\theta\in L^q(\Omega_0)^3$ with $3/s+1/q\leq 1$, as used in [22] for the two-field mixed method), but a complete existence theory is still an open question. We proceed under the assumptions that the hyperbolic initial/boundary-value problem in question admits a solution in some sense in spaces defined above, and given this, we continue to construct the numerical approximation of the solution, and replace the continuous spaces by their discrete counterparts.

2.2. Domain decomposition

To allow for different time steps/integrators to be used in different regions of the domain Ω, we use the dual domain decomposition method since it is easily parallelizable. We adopt the method of local Lagrange multipliers, introduced by Park et al. [36], where each domain is constrained to an intermediate interface, Σ, as shown in Fig. 3.
This method is favorable for non-conforming meshes as presented by Brezzi and Marini [9] and Park et al. [37], and eliminates over-constraints where more than two subdomains meet.

The augmented Lagrange function and augmented action integral yield

$$\hat{L}(\boldsymbol{u},\dot{\boldsymbol{u}},\theta,p,\boldsymbol{\lambda},w)=T(\dot{\boldsymbol{u}})-V(\boldsymbol{u},\theta,p)+\sum_{k=1}^{N_D}\int_{\Gamma^k}\Phi^k(\boldsymbol{u},\boldsymbol{w})^T\boldsymbol{\lambda}^k dS_0,\quad \hat{A}(\boldsymbol{u},\theta,p,\boldsymbol{\lambda},\boldsymbol{w})=A(\boldsymbol{u},\theta,p)+\int_{t_1}^{t_2}\sum_{k=1}^{N_D}\int_{\Gamma^k}\Phi^k(\boldsymbol{u},\boldsymbol{w})^T\boldsymbol{\lambda}^k dS_0 dt, \tag{14}$$

and the constraint function is defined as

$$\Phi^k(\boldsymbol{u},\boldsymbol{w})=\boldsymbol{u}^k-\boldsymbol{w}^k=\boldsymbol{B}^k\boldsymbol{u}-\boldsymbol{D}^k\boldsymbol{w}=0, \tag{15}$$

where the operators $\boldsymbol{B}^k$ and $\boldsymbol{D}^k$ are the Boolean matrices extracting the interface degrees of freedom from $\boldsymbol{u}$ and the corresponding degrees of freedom from $\boldsymbol{w}$ for a particular subdomain k. The relationship between the constraint on displacements, used in this work, or velocities, used by Prakash and Hjelmstad [38], is explained in Appendix A.

The Euler-Lagrange equations resulting from this augmented action integral for the asynchronous case, which is the main objective of this paper, are presented in what follows.

3. Discrete asynchronous multi-domain integrators

Since the stability and accuracy requirements for different domains may necessitate different time step sizes, we developed a discrete multi-domain asynchronous variational integrator, where each domain advances with its own step size and integrator (explicit/implicit). To formulate such integrators, we follow our earlier work focused on ODEs [18]. More details on discrete variational integrators can also be found in [31,42,43].

3.1. Spatial discretization

We begin by traditional discretization in space by the finite element method:

$$\begin{aligned}
&\boldsymbol{u}^h=\Psi_u^T\tilde{\boldsymbol{u}},\quad \boldsymbol{u}^h\big|_{\Omega_e}=\sum_{i=1}^{NN_u}\Psi_u^i(\boldsymbol{x})\tilde{\boldsymbol{u}}^i(t),\quad \forall\boldsymbol{u}^h\in H^h\subset H^{1,2},\\
&\theta^h=\Psi_\theta^T\tilde{\theta},\quad \theta^h\big|_{\Omega_e}=\sum_{i=1}^{NN_\theta}\Psi_\theta^i(\boldsymbol{x})\tilde{\theta}^i(t),\quad \forall\theta^h\in L^h\subset L^2(\Omega_0),\\
&p^h=\Psi_p^T\tilde{\mathrm{p}},\quad p^h\big|_{\Omega_e}=\sum_{i=1}^{NN_p}\Psi_p^i(\boldsymbol{x})\tilde{p}^i(t),\quad \forall p^h\in L^h\subset L^2(\Omega_0).
\end{aligned} \tag{16}$$

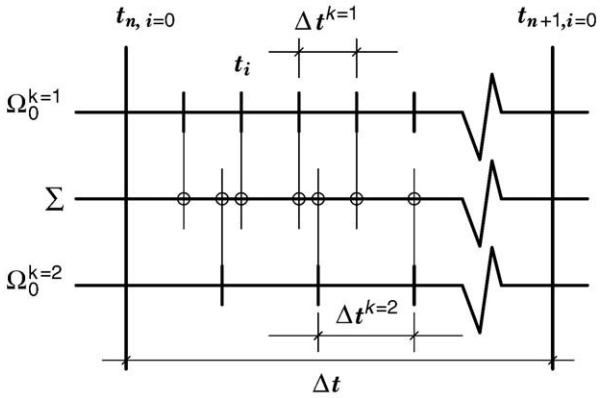

Fig. 4. Substeps of the system time step.

The interface motion and the corresponding Lagrange multipliers are approximated as follows:

$$\boldsymbol{w}^h = \Xi_w\,\tilde{\boldsymbol{w}},\quad \boldsymbol{w}^h|_\Sigma = \sum_{i=1}^{NN_w}\Xi_w^i(\boldsymbol{x})\,\tilde{\mathrm{w}}i(t),\quad \forall \boldsymbol{w}^h\in\Phi^h\subset W^{\frac{1}{2},2}(\Sigma)^3,\ \boldsymbol{\lambda}^h = \Xi_{\boldsymbol{\lambda}}\,\tilde{\boldsymbol{\lambda}},\quad \boldsymbol{\lambda}^h|_\Sigma = \sum_{i=1}^{NN_\lambda}\Xi_{\boldsymbol{\lambda}}^i(\boldsymbol{x})\,\tilde{\lambda}^i(t),\quad \forall \boldsymbol{\lambda}^h\in M^h\subset W^{-\frac{1}{2},2}(\Sigma)^3. \tag{17}$$

Here, we denote by H^h and L^h the finite element subspace of the space $H^{1,2}$ and $L^2(\Omega_0)$, respectively. The finite element trace space Φ^h and M^h are the subspaces of $W^{\frac{1}{2},2}(\Sigma)^3$ and $W^{-\frac{1}{2},2}(\Sigma)^3$.

3.2. Asynchronous Lagrangian framework

To facilitate the discussion on asynchronous time stepping, we start by introducing a generalized midpoint rule for primary unknowns

$$\begin{aligned}
\boldsymbol{u}^h_{n+\alpha} &= (1-\alpha)\boldsymbol{u}^h_n + \alpha\boldsymbol{u}^h_{n+1},\\
\theta^h_{n+\alpha} &= (1-\alpha)\theta^h_n + \alpha\theta^h_{n+1},\\
p^h_{n+\alpha} &= (1-\alpha)p^h_n + \alpha p^h_{n+1}.
\end{aligned} \tag{18}$$

The discrete deformation gradient now reads

$$\boldsymbol{F}_{n+\alpha} = (1-\alpha)\boldsymbol{F}_n + \alpha\boldsymbol{F}_{n+1} = (1-\alpha)\left(1+\nabla_0\boldsymbol{u}^h_n\right) + \alpha\left(1+\nabla_0\boldsymbol{u}^h_{n+1}\right), \tag{19}$$

where $\mathbf{1}$ is the second order identity tensor.

Next, we decompose domain, $\Omega_0 = \cup_{k=1}^{N_D}\Omega_0^k$ (see Fig. 3), and introduce a substep time $\Delta t^k = \Delta t/s^k$, which is proportional to the system time step $\Delta t = t_{n+1} - t_n$, where s^k is the number of substeps for domain k, as shown schematically in Fig. 4.

As in the continuous case, the *discrete augmented Lagrangian* is a map that approximates the augmented Lagrangian Eq. (14) over the one system time step

$$\hat{L}_d\left(\boldsymbol{u}^h_n,\boldsymbol{u}^h_{n+1},\theta^h_n,\theta^h_{n+1},p^h_n,p^h_{n+1},\boldsymbol{\lambda}^h_n,\boldsymbol{w}^h_n\right)\approx\int_{t_n}^{t_{n+1}}\hat{L}_h\left(\boldsymbol{u}^h,\dot{\boldsymbol{u}}^h,\theta^h,p^h,\boldsymbol{\lambda}^h,\boldsymbol{w}^h\right)\mathrm{d}t. \tag{20}$$

Employing the generalized midpoint rule, Eq. (18), and taking into consideration a substep Δt^k, the *discrete augmented Lagrangian* $\hat{L}^k_d(\boldsymbol{u}^h_i, \boldsymbol{u}^h_{i+1}, \theta^h_i, \theta^h_{i+1}, p^h_i, p^h_{i+1}, \boldsymbol{\lambda}^h_i, \boldsymbol{w}^h_i)$ for one subdomain with its own substep time yields

$$\hat{L}^k_d = \Delta t^k\,\hat{L}^k_h\left(\boldsymbol{u}_{i+\alpha},\frac{\boldsymbol{u}^h_{i+1}-\boldsymbol{u}^h_i}{\Delta t^k},\theta^h_{i+\alpha},p^h_{i+\alpha},\boldsymbol{\lambda}^h_i,\boldsymbol{w}^h_i\right), \tag{21}$$

where $\bullet_i = \bullet(t_n + i\Delta t^k)$ and $\bullet_{i+\alpha} = (1-\alpha)\,\bullet_i + \alpha\bullet_{i+1}$ (Fig. 4). Following the three-field continuous case, Eqs. (4)–(6), with the domain decomposition, Eqs. (14) and (15), the *discrete augmented Lagrangian* for subdomain k and substep Δt^k reads

$$\begin{aligned}
\hat{L}^k_d = \Delta t^k\Bigg\{&\frac{1}{2}\int_{\Omega^k_0}\rho_0\left(\frac{\boldsymbol{u}^h_{i+1}-\boldsymbol{u}^h_i}{\Delta t^k}\right)\cdot\left(\frac{\boldsymbol{u}^h_{i+1}-\boldsymbol{u}^h_i}{\Delta t^k}\right)d\Omega^k_0 - \int_{\Omega^k_0}\left\{\widehat{W}(\boldsymbol{C}_{i+\alpha}) + U\left(\theta^h_{i+\alpha}\right)\right\}d\Omega^k_0 - \int_{\Omega^k_0}p^h_{i+\alpha}\left(J_{i+\alpha}-\theta^h_{i+\alpha}\right)d\Omega^k_0\\
&+\int_{\Omega^k_0}(\boldsymbol{f}_0)_{i+\alpha}\cdot\boldsymbol{u}^h_{i+\alpha}d\Omega^k_0 + \int_{\partial\Omega^k_p}(\bar{\boldsymbol{t}}_0)_{i+\alpha}\cdot\boldsymbol{u}^h_{i+\alpha}dS_0 + \int_{\Gamma^k}\boldsymbol{\Phi}^k\left(\boldsymbol{u}^h_i,\boldsymbol{w}^h_i\right)^T\left(\boldsymbol{\lambda}^h_i\right)^k dS_0\Bigg\}.
\end{aligned} \tag{22}$$

The total *discrete augmented Lagrangian* for a whole body and the corresponding *discrete augmented action sum* are given by summation over all substeps (s^k), all subdomains (N_D) and all time intervals (N_T):

$$\hat{L}_d = \sum_{r=1}^{N_D}\sum_{i=1}^{s^k-1}\hat{L}^k_d\left(\boldsymbol{u}^h_i,\boldsymbol{u}^h_{i+1},\theta^h_i,\theta^h_{i+1},p^h_i,p^h_{i+1},\boldsymbol{\lambda}^h_i,\boldsymbol{w}^h_i\right),\quad \hat{A}d = \sum_{n=0}^{N_T-1}\sum_{r=1}^{N_D}\sum_{i=1}^{s^k-1}\hat{L}^k_d\left(\boldsymbol{u}^h_i,\boldsymbol{u}^h_{i+1},\theta^h_i,\theta^h_{i+1},p^h_i,p^h_{i+1},\boldsymbol{\lambda}^h_i,\boldsymbol{w}^h_i\right). \tag{23}$$

In this paper, the position of the common interface $\boldsymbol{w}^h$ separating the subdomain Ω^k and the supplement $\Omega-\Omega^k$ is linearly interpolated by

$$\boldsymbol{w}^h_i = \left(1-\frac{i}{s^k}\right)\boldsymbol{w}^h_n + \left(\frac{i}{s^k}\right)\boldsymbol{w}^h_{n+1},\quad \forall i = 1,\ldots,s^k. \tag{24}$$

Note that different interface motion interpolations, $\boldsymbol{w}^h_i$, will likely lead to a different response of the integrator and potentially its conservation/stability criteria.

Similar to the continuous case, the discrete Hamilton's principle states that the motion makes the discrete action sum stationary $\delta\hat{A}_d = 0$. This leads to system of s^k discrete Euler-Lagrange equations for $\boldsymbol{u}^h$, θ^h and p^h:

$$\begin{aligned}
&\frac{\partial}{\partial \boldsymbol{u}_i^h}\hat{L}_d^k\left(\boldsymbol{u}_{i-1}^h,\boldsymbol{u}_i^h,\theta_{i-1}^h,\theta_i^h,p_{i-1}^h,p_i^h,\boldsymbol{\lambda}_{i-1}^h,\boldsymbol{w}_n^h,\boldsymbol{w}_{n+1}^h\right)+\frac{\partial}{\partial \boldsymbol{u}_i^h}\hat{L}_d^k\left(\boldsymbol{u}_i^h,\mathrm{u}_{i+1}^h,\theta_i^h,\theta_{i+1}^h,p_i^h,p_{i+1}^h,\boldsymbol{\lambda}_i^h,\boldsymbol{w}_n^h,\boldsymbol{w}_{n+1}^h\right)=0,\\
&\frac{\partial}{\partial \theta_i^h}\hat{L}_d^k\left(\boldsymbol{u}_{i-1}^h,\boldsymbol{u}_i^h,\theta_{i-1}^h,\theta_i^h,p_{i-1}^h,p_i^h,\boldsymbol{\lambda}_{i-1}^h,\boldsymbol{w}_n^h,\boldsymbol{w}_{n+1}^h\right)+\frac{\partial}{\partial \theta_i^h}\hat{L}_d^k\left(\boldsymbol{u}_i^h,\boldsymbol{u}_{i+1}^h,\theta_i^h,\theta_{i+1}^h,p_i^h,p_{i+1}^h,\boldsymbol{\lambda}_i^h,\boldsymbol{w}_n^h,\boldsymbol{w}_{n+1}^h\right)=0,\\
&\frac{\partial}{\partial p_i^h}\hat{L}_d^k\left(\boldsymbol{u}_{i-1}^h,\boldsymbol{u}_i^h,\theta_{i-1}^h,\theta_i^h,p_{i-1}^h,p_i^h,\boldsymbol{\lambda}_{i-1}^h,\boldsymbol{w}_n^h,\boldsymbol{w}_{n+1}^h\right)+\frac{\partial}{\partial p_i^h}\hat{L}_d^k\left(\boldsymbol{u}_i^h,\boldsymbol{u}_{i+1}^h,\theta_i^h,\theta_{i+1}^h,p_i^h,p_{i+1}^h,\boldsymbol{\lambda}_i^h,\boldsymbol{w}_n^h,\boldsymbol{w}_{n+1}^h\right)=0.
\end{aligned}\tag{25}$$

s^k equations for Lagrange multipliers constraining domain Ω^k to the interface Σ at each substep:

$$\frac{\partial}{\partial \boldsymbol{\lambda}_{i+1}^h}\hat{L}_d^k\left(\boldsymbol{u}_{i+1}^h,\boldsymbol{u}_{i+2}^h,\theta_{i+1}^h,\theta_{i+2}^h,p_{i+1}^h,p_{i+2}^h,\boldsymbol{\lambda}_{i+1}^h,\boldsymbol{w}_n^h,\boldsymbol{w}_{n+1}^h\right)=0,\tag{26}$$

and for the interface we have

$$\frac{\partial}{\partial \boldsymbol{w}_n^h}\hat{L}_d^k\left(\boldsymbol{u}_i^h,\boldsymbol{u}_{i+1}^h,\theta_i^h,\theta_{i+1}^h,p_i^h,p_{i+1}^h,\boldsymbol{\lambda}_i^h,\boldsymbol{w}_{n-1}^h,\boldsymbol{w}_n^h\right)+\frac{\partial}{\partial \boldsymbol{w}_n^h}\hat{L}_d^k\left(\boldsymbol{u}_i^h,\boldsymbol{u}_{i+1}^h,\theta_i^h,\theta_{i+1}^h,p_i^h,p_{i+1}^h,\boldsymbol{\lambda}_i^h,\boldsymbol{w}_n^h,\boldsymbol{w}_{n+1}^h\right)=0.\tag{27}$$

The above equation represents a weak form of the force balance at the subdomain interfaces.

The residual form of the discrete Euler-Lagrange Eqs. (25)–(27) prevalent for the numerical implementation is given by

$$\begin{aligned}
\mathscr{R}_{\mathrm{u}} = &-\int_{\Omega_0^k}\rho_0\left(\frac{\boldsymbol{u}_{i+1}^h-2\boldsymbol{u}_i^h+\boldsymbol{u}_{i-1}^h}{\Delta t^k}\right)\cdot\delta\boldsymbol{u}^h\mathrm{d}\Omega_0^k\\
&-\alpha\Delta t^k\int_{\Omega_0^k}\hat{\boldsymbol{S}}'_{i-1+\alpha}:\left[\boldsymbol{F}_{i-1+\alpha}^T(\nabla_0\delta\boldsymbol{u}^h)\right]\mathrm{d}\Omega_0^k-\alpha\Delta t^k\int_{\Omega_0^k}p_{i-1+\alpha}^h J_{i-1+\alpha}\mathrm{C}_{i-1+\alpha}^{-1}:\left[\boldsymbol{F}_{i-1+\alpha}^T(\nabla_0\delta\boldsymbol{u}^h)\right]\mathrm{d}\Omega_0^k\\
&-(1-\alpha)\Delta t^k\int_{\Omega_0^k}\hat{\boldsymbol{S}}'_{i+\alpha}:\left[\boldsymbol{F}_{i+\alpha}^T(\nabla_0\delta\boldsymbol{u}^h)\right]\mathrm{d}\Omega_0^k-(1-\alpha)\Delta t^k\int_{\Omega_0^k}p_{i+\alpha}^h J_{i+\alpha}\mathrm{C}_{i+\alpha}^{-1}:\left[\boldsymbol{F}_{i+\alpha}^T(\nabla_0\delta\boldsymbol{u}^h)\right]\mathrm{d}\Omega_0^k\\
&+\alpha\Delta t^k\int_{\Omega_0^k}(\boldsymbol{f}_0)_{i-1+\alpha}\cdot\delta\boldsymbol{u}^h\mathrm{d}\Omega_0^k+(1-\alpha)\Delta t^k\int_{\Omega_0^k}(\boldsymbol{f}_0)_{i+\alpha}\cdot\delta\boldsymbol{u}^h\mathrm{d}\Omega_0^k+\alpha\Delta t^k\int_{\partial\Omega_p}(\bar{\mathrm{t}}_0)_{i-1+\alpha}\cdot\delta\boldsymbol{u}^h\mathrm{d}S_0\\
&+(1-\alpha)\Delta t^k\int_{\partial\Omega_p}(\bar{\mathrm{t}}_0)_{i+\alpha}\cdot\delta\boldsymbol{u}^h\mathrm{d}S_0+\Delta t^k\int_{\Gamma^k}\mathrm{B}^k(\delta\boldsymbol{u}^h)^T(\boldsymbol{\lambda}_i^h)^k\mathrm{d}S_0=0,\\
\mathscr{R}_\theta = &-\Delta t^k\int_{\Omega_0^k}\left[\kappa\alpha\left(\theta_{i-1+\alpha}^h-1\right)+\kappa(1-\alpha)\left(\theta_{i+\alpha}^h-1\right)\right]\delta\theta^h\mathrm{d}\Omega_0^k+\Delta t^k\int_{\Omega_0^k}\left[\alpha p_{i-1+\alpha}^h+(1-\alpha)p_{i+\alpha}^h\right]\delta\theta^h\mathrm{d}\Omega_0^k=0,\\
\mathscr{R}_p = &-\Delta t^k\int_{\Omega_0^k}\left[\alpha J_{i-1+\alpha}+(1-\alpha)J_{i+\alpha}\right]\delta p^h\mathrm{d}\Omega_0^k+\Delta t^k\int_{\Omega_0^k}\left[\alpha\theta_{i-1+\alpha}^h+(1-\alpha)\theta_{i+\alpha}^h\right]\delta p^h\mathrm{d}\Omega_0^k=0,
\end{aligned}\tag{28}$$

with

$$\mathscr{R}_{\boldsymbol{\lambda}}=\Delta t^k\int_{\Gamma^k}\left[\boldsymbol{B}^k\left(\boldsymbol{u}_{i+1}^h\right)^T-\left(1-\frac{i+1}{s^k}\right)\boldsymbol{D}^k\left(\boldsymbol{w}_n^h\right)^T-\left(\frac{i+1}{s^k}\right)\boldsymbol{D}^k\left(\boldsymbol{w}_{n+1}^h\right)^T\right]\cdot\delta\boldsymbol{\lambda}^h\mathrm{d}S_0=0,\tag{29}$$

and for the interface we get

$$\mathscr{R}_{\boldsymbol{w}}=\sum_{k=1}^{N_D}\sum_{i=0}^{s^k-1}\Delta t^k\int_{\Gamma^r}\left[-\left(\frac{i}{s^k}\right)\boldsymbol{D}^k\left(\delta\boldsymbol{w}^h\right)^T\cdot\left(\boldsymbol{\lambda}^h\right)_{n-1,i}^k-\left(1-\frac{i}{s^k}\right)\boldsymbol{D}^k\left(\delta\boldsymbol{w}^h\right)^T\cdot\left(\boldsymbol{\lambda}_i^h\right)^k\right]\mathrm{d}S_0=0,\tag{30}$$

where $\delta\boldsymbol{u}^h\in H^h\subset H^{1,2}$, $\delta\theta^h\in L^h\subset L^2(\Omega_0)$, $\delta p^h\in L^h\subset L^2(\Omega_0)$, $\delta\boldsymbol{w}^h\in\Phi^h\subset W^{\frac{1}{2},2}(\Sigma)^3$, $\delta\boldsymbol{\lambda}^h\in M^h\subset W^{-\frac{1}{2},2}(\Sigma)^3$ and $(\lambda^h)_{n-1,i}^k=(\lambda^h)^k(t_{n-1}+i\Delta t^k)$. Note that $(\lambda_i^h)^k\equiv(\lambda^h)_{n,i}^k=(\lambda^h)^k(t_n+i\Delta t^k)$ (see Fig. 4). For synchronous time stepping $s^k=1$, one can substitute n for i and all equations will collapse to a simple form with Δt as a single time step.

3.3. Consistent linearization

As usual for a nonlinear problem, the system (Eqs. (28)–(30)) must be solved using some iterative technique, such as Newton's method. Consistent linearization is required if one wants to achieve the quadratic rate of convergence. We show the general structure of the Jacobian

matrix derived by consistent linearization of residuals (28), (29) and (30), which has a block-bordered form amenable to parallel computation, with each block assigned to a different processor:

$$J_g(y) = \left(\frac{\mathcal{A}_{11} \,|\, \mathcal{A}_{12}}{\mathcal{A}_{12}^T \,|\, \mathcal{A}_{22}}\right), \tag{31}$$

where

$$\mathcal{A}_{11} = \left(\begin{array}{cccccc|c|c} \mathsf{K}^1 & 0 & 0 & 0 & \cdots & 0 & & \\ \mathsf{L}^2 & \mathsf{K}^2 & 0 & 0 & \cdots & 0 & & \\ \mathsf{N}^3 & \mathsf{L}^3 & \mathsf{K}^3 & 0 & \cdots & 0 & & \\ 0 & \mathsf{N}^4 & \mathsf{L}^4 & \mathsf{K}^4 & \ddots & \vdots & & \\ \vdots & \ddots & \ddots & \ddots & \ddots & 0 & & \\ 0 & \cdots & 0 & \mathsf{N}^{s^k} & \mathsf{L}^{s^k} & \mathsf{K}^{s^k} & & \\ \hline & & & & & & \ddots & \\ \hline & & & & & & & \end{array}\right),$$

and

$$\mathcal{A}_{12}^T = \left(\begin{array}{cccccc|c|c} C_{\lambda u}^T & 0 & \cdots & & & 0 & & \\ 0 & C_{\lambda u}^T & 0 & \cdots & & 0 & & \\ 0 & 0 & C_{\lambda u}^T & 0 & \cdots & 0 & & \\ \vdots & & \ddots & \ddots & \ddots & \vdots & & \\ 0 & & \cdots & 0 & C_{\lambda u}^T & 0 & & \\ 0 & & & \cdots & 0 & C_{\lambda u}^T & & \\ \hline & & & & & & \ddots & \\ \hline 0 & & & & \cdots & 0 & \cdots & \end{array}\right),$$

and

$$\mathcal{A}_{22} = \left(\begin{array}{ccccccc|c} 0 & \cdots & & & \cdots & 0 & & -\frac{1}{s^k}\mathsf{C}_{\lambda w} \\ \vdots & \ddots & & & & \vdots & & -\frac{2}{s^k}\mathsf{C}_{\lambda w} \\ & & & & & & & -\frac{3}{s^k}\mathsf{C}_{\lambda w} \\ & & & & & & & \vdots \\ \vdots & & & & \ddots & \vdots & & -\frac{s^k-1}{s^k}\mathsf{C}_{\lambda w} \\ 0 & \cdots & & & \cdots & 0 & & -\mathsf{C}_{\lambda w} \\ \hline & & & & & & \ddots & \vdots \\ \hline \mathsf{C}_{\lambda w}^{\mathsf{T}} & \frac{s^k-1}{s^k}\mathsf{C}_{\lambda w}^{\mathsf{T}} & \cdots & \frac{3}{s^k}\mathsf{C}_{\lambda w}^{\mathsf{T}} & \frac{2}{s^k}\mathsf{C}_{\lambda w}^{\mathsf{T}} & \frac{1}{s^k}\mathsf{C}_{\lambda w}^{\mathsf{T}} & \cdots & 0 \end{array}\right).$$

The solution vector $\boldsymbol{y}$ is assembled as

$$\boldsymbol{y}^T = \Big(\underbrace{\boldsymbol{u}_1^h, \theta_1^h, p_1^h,}_{\text{Domain } k=1} \underbrace{\boldsymbol{u}_1^h, \theta_1^h, p_1^h, \boldsymbol{u}_2^h, \theta_2^h, p_2^h}_{\text{Domain } k=2} \underbrace{\left(\boldsymbol{\lambda}_0^h\right)^{k=1}, \left(\boldsymbol{\lambda}_0^h\right)^{k=2}, \left(\boldsymbol{\lambda}_1^h\right)^{k=2}, \mathbf{w}_1}_{\text{Interface}}\Big) \tag{32}$$

for a simple two domain problem with $s^{k=1}=1$ and $s^{k=2}=2$, for example.

Individual matrices K^i, L^i and N^i are derived by consistent linearization of a particular residual with $i+1$, i and $i-1$ substeps:

$$K^i = \begin{pmatrix} K^i_{uu} & 0 & (K^i_{pu})^T \\ 0 & K^i_{\theta\theta} & (K^i_{p\theta})^T \\ K^i_{pu} & K^i_{p\theta} & 0 \end{pmatrix}, i = 1,\ldots,s^k, K^i_{\square\triangle} = \frac{\partial.\mathscr{R}\square}{\partial\Delta_{i+1}}, \tag{33}$$

$$L^i = \begin{pmatrix} L^i_{uu} & 0 & \left(L^i_{pu}\right)^T \\ 0 & L^i_{\theta\theta} & \left(L^i_{p\theta}\right)^T \\ L^i_{pu} & L^i_{p\theta} & 0 \end{pmatrix}, i = 2,\ldots,s^k, L^i_{\square\triangle} = \frac{\partial.\mathscr{R}\square}{\partial\Delta_i}, \tag{34}$$

$$N^i = \begin{pmatrix} N^i_{uu} & 0 & \left(N^i_{pu}\right)^T \\ 0 & N^i_{\theta\theta} & \left(N^i_{p\theta}\right)^T \\ N^i_{pu} & N^i_{p\theta} & 0 \end{pmatrix}, i = 3,\ldots,s^k, N^i_{\square\triangle} = \frac{\partial.\mathscr{R}\square}{\partial\Delta_{i-1}}. \tag{35}$$

Note that $\forall i = 3,\ldots,s^k$ we get the equivalence $N^i = K^{i-1}$. All the individual linearized components including the coupling matrices $C_{\lambda u}$ and $C_{\lambda w}$ are given in Appendix B.

Several interesting features can be observed when investigating Eq. (31). After standard mathematical operations, the matrix (31) can be transformed to a dual–primal system, which relates the dual Lagrange multipliers $\boldsymbol{\lambda}^h$ to quasi-primary interface displacement degrees of freedom $\mathbf{w}^h$, similar to that from FETI-DP [15]. Once the local Lagrange multipliers $\boldsymbol{\lambda}^h$ and interface displacements $\mathbf{w}^h$ are known, one can easily evaluate the true primary variables $(\mathbf{u}^h, \theta^h, p^h)$ since the internal block, $\mathcal{A}_{11}$, is a lower triangular matrix that can be solved by forward substitution row-wise from top to bottom which simply amounts to time stepping the initial state $\mathbf{u}^h_n$, θ^h_n and p^h_n by s^k time steps $i\forall N_D$. This operation can be performed with great efficiency in parallel, and for an explicit integrator will lead to a standard recursion formula when a lumped mass matrix is used. Moreover, for synchronous time steps and lower order elements, such as $Q_1/P_0/V_0$, we can simply statically condense the pressure and the volumetric unknown to get:

$$J_g(y) = \left(\begin{array}{c|c|cc} \overline{K} & & C^T_{\lambda u} & 0 \\ \hline & \ddots & & \\ \hline C^T_{\lambda u} & & 0 & C_{\lambda w} \\ 0 & & C^T_{\lambda w} & 0 \end{array}\right), \tag{36}$$

where

$$\overline{K} = \left[K_{uu} + K^T_{pu}\left(K_{p\theta}K^{-1}_{\theta\theta}K^T_{p\theta}\right)^{-1}K_{pu}\right]. \tag{37}$$

The residual vector is given by

$$-\overline{\mathcal{R}}_u = -\mathcal{R}_u + K^T_{pu}K^{-1}_{p\theta}\mathcal{R}_\theta - K^T_{pu}\left(K_{p\theta}K^{-1}_{\theta\theta}K^T_{p\theta}\right)^{-1}\mathcal{R}_p, \tag{38}$$

where $\mathscr{R}_u = \mathcal{R}_u \cdot \delta\mathbf{u}^h$, $\mathscr{R}_\theta = \mathcal{R}_\theta \cdot \delta\theta^h$ and $\mathscr{R}_p = \mathcal{R}_p \cdot \delta p^h$. However, the static condensation becomes more complicated for asynchronous case since p^h_{i+1} depends on p^h_i and p^h_{i-1} in a non-trivial fashion. Similar complex relationships hold for θ^h. In this work, we solve for all unknowns simultaneously by a monolithic method using a direct solver [12]. This monolithic implementation makes our integrators computationally non-optimal, for some applications, and a solution strategy similar to that adopted in FETI-DP [15] will be important, especially in a 3D setting. In our initial work, we have not focused on this efficient implementation, but rather on the mathematical and physical characteristics of our integrator, such as consistency, order of convergence, energy conservation, etc.

4. Conservation analysis

Here, we focus on energy conservation properties of our asynchronous integrators. Note that since we discretize the mixed variational principle, the conservation properties are not fully known. We investigate the generalized midpoint rule ($\alpha = 1/2$) and assess its discrete energy evolution, since the energy dissipation is widely regarded as a natural criterion of stability [21,22,38]. Note that we make no claims about the stability of our midpoint integrator, in this section, since it is known that energy conservation is not sufficient for numerical stability in the nonlinear range [35]. For linear stability analysis of AVI, we point the interested reader to work of Fong et al. [17]. The external forces are considered zero without loss of generality in this section.

As has been reported by Hauret and Le Tallec [22], for a standard consistent integrator one can derive an energy error estimate

$$E_{n+1/2} - E_{n-1/2} = c_n \Delta t^q, \tag{39}$$

where q is typically an exponent of second or third-order and the constant c_n dependents on material properties, size of the domain, level of the discretization, etc., [22]. However, for the asynchronous time stepping presented in this work, the interface force balance *is not* satisfied time-wise for an arbitrary substep i even when we "synchronize" at the system time step n (Fig. 5(b)). Rather, we enforce the linear momentum balance weakly in the space–time domain, Eq. (30), as in the space–time discountinous Galerkin method [1]. Take for example the two domain problem shown in Fig. 5(b). The force balance at the system time step reads

$$\left(\boldsymbol{\lambda}^h\right)^b_n = -\frac{1}{4}\left(\boldsymbol{\lambda}^h\right)^a_{n,0} - \frac{1}{16}\left(\boldsymbol{\lambda}^h\right)^a_{n-1,1} - \frac{3}{16}\left(\boldsymbol{\lambda}^h\right)^a_{n,1} - \frac{1}{8}\left(\boldsymbol{\lambda}^h\right)^a_{n-1,2} - \frac{1}{8}\left(\boldsymbol{\lambda}^h\right)^a_{n,2} - \frac{3}{16}\left(\boldsymbol{\lambda}^h\right)^a_{n-1,3} - \frac{1}{16}\left(\boldsymbol{\lambda}^h\right)^a_{n,3}. \tag{40}$$

Therefore, we present hereafter an energy evolution criterion, similar to one given by Eq. (39), but for the asynchronous midpoint method presented in this work. We follow the approach by Hauret and Le Tallec [22], and provide a detailed derivation in Appendix C. For the common interface (24), one can derive the following global energy error estimate:

$$\overline{\mathcal{E}}_t = \sum_{k=1}^{N_D}\sum_{i=0}^{s^k-1}\left(\frac{i}{s^k}\right)\Delta\mathcal{E}^k_{n-1,i} + \left(1-\frac{i}{s^k}\right)\Delta\mathcal{E}^k_{n,i} = \tilde{c}_n\Delta t^3. \tag{41}$$

Note that Eq. (41) represents a sum of unbalanced energy projections (Eq. (C.15)) between ${}_{n-1,i}$ ($\Delta\mathcal{E}^k_{n-1,i}$) and ${}_{n,i}$ ($\Delta\mathcal{E}^k_{n,i}$) substeps over a system time step Δt, where the projection surface coincides with the linear constraint interpolation (Eq. (24)).

Although the global energy conservation described above is promising, we are still interested in the local energy evolution, from ${}_{i-1/2}$ to ${}_{i+1/2}$, as in the synchronous case Eq. (C.12). We start by rewriting Eq. (C.9) in the incremental form

$$\Delta\mathcal{E}^k_i = \Delta t^k\int_{\Gamma^k}\left(\boldsymbol{B}^k\left(\frac{\phi^h_{i+1}-\phi^h_{i-1}}{2\Delta t^k}\right)\right)^T\left(\boldsymbol{\lambda}^h_i\right)^k \mathrm{d}S_0 + c_i\left(\Delta t^k\right)^3, \tag{42}$$

and employing the recurrent formula

$$\begin{aligned}\Delta\mathcal{E}^k_i &= \Delta t^k\int_{\Gamma^k}\left(\boldsymbol{B}^k\left(\dot{\boldsymbol{u}}^h_i\right)\right)^T\left(\boldsymbol{\lambda}^h_i\right)^k \mathrm{d}S_0 + c_i\left(\Delta t^k\right)^3,\\ \Delta\mathcal{E}^k_{i-1} &= \Delta t^k\int_{\Gamma^k}\left(\boldsymbol{B}^k\left(\dot{\boldsymbol{u}}^h_i\right)\right)^T\left(\boldsymbol{\lambda}^h_{i-1}\right)^k \mathrm{d}S_0 + c_i\left(\Delta t^k\right)^2.\end{aligned} \tag{43}$$

Then,

$$\Delta\mathcal{E}^k_i - \Delta\mathcal{E}^k_{i-1} = \left(\Delta t^k\right)^2\int_{\Gamma^k}\left(\boldsymbol{B}^k\left(\dot{\boldsymbol{u}}^h_i\right)\right)^T\left(\dot{\boldsymbol{\lambda}}^h_i\right)^k \mathrm{d}S_0 + c_i\left(\Delta t^k\right)^2, \tag{44}$$

and using mathematical induction one gets

$$E^k_{i+\frac{1}{2}} - E^k_{i-\frac{1}{2}} = c_i\left(\Delta t^k\right)^2, \tag{45}$$

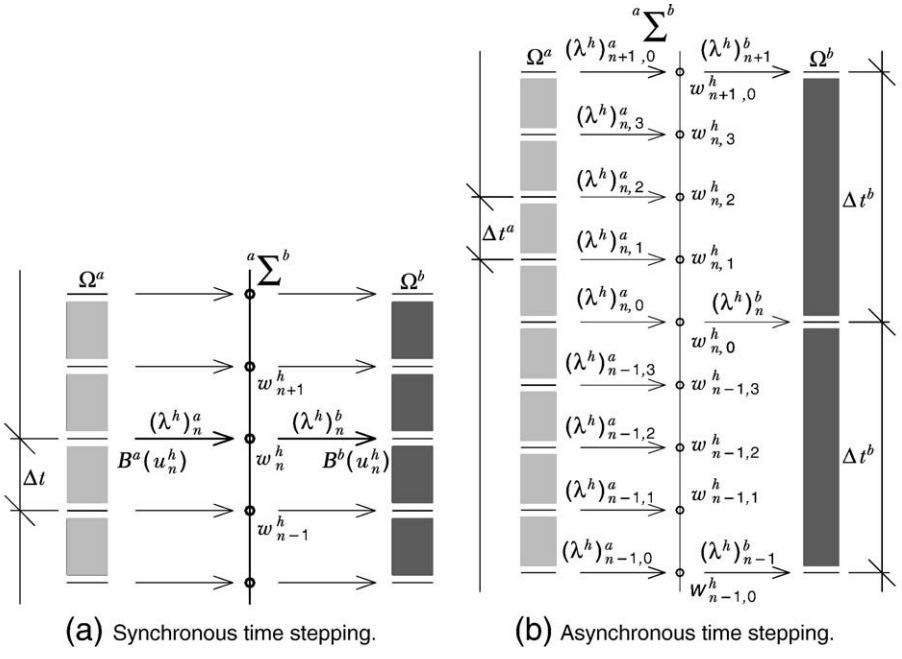

Fig. 5. Balance of Lagrange multipliers across a common interface. Note that in general $\Delta t^a \neq \Delta t^b \neq \Delta t$.

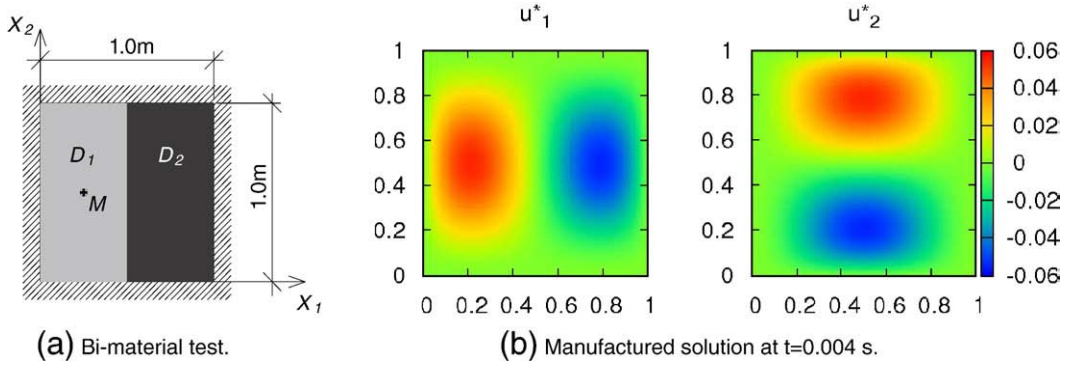

Fig. 6. Method of manufactured solutions for an incompressible material.

since conservative mechanical systems are typically used in the stability studies, $\Delta E^k_{i-1}=0|_{t=0}$ (see [24] for more details). Note that Eq. (45) holds regardless of how the common interface is interpolated. Also, the estimate Eq. (45) is the strictest estimate on the local energy balance, and does not preclude the superior conservation in reality. However, using the theory just presented, we were not able to derive the higher order local criterion. Some physical interpretations for the above estimates (41) and (45) are presented in Section 5.2.

5. Numerical examples

In this section, convergence tests, the stability study and the analysis of the error decay due to asynchronous time stepping are performed to assess performance of numerical methodologies developed in this work. The convergence study is used to examine consistency of the formulation while energy conservation is performed to investigate stability of the integrators. Finally, we solve the problem with mixed integration (implicit/explicit) and lastly show the potential of our method for engineering applications. The finite elements considered for these studies are classical two-dimensional plane strain $Q_1/P_0/V_0$ elements, where displacement field is bi-linear, and pressure and volume are constant over the element. The Lagrange multiplier field is selected to be linear over the element edge in this study.

5.1. Convergence study

In this subsection, we perform the convergence study on a bi-material system to investigate the consistency of the proposed asynchronous integrators. Both space and time convergence tests are performed using the Method of Manufactured Solutions (MMS). We select a solution that satisfies the incompressibility constraint, $\nabla\cdot\boldsymbol{u}^*=0$, albeit in the small strain setting. The manufactured solution reads

$$u_1^*(X_1,X_2,t) = -10X_1(1-X_1)(1-2X_1)X_2^2(1-X_2)^2\mathcal{M}_1(t),$$
$$u_2^*(X_1,X_2,t) = 10X_1^2(1-X_1)^2X_2(1-X_2)(1-2X_2)\mathcal{M}_1(t), \tag{46}$$

where

$$\mathcal{M}_1(t) = \left[\frac{cos(10^3t-\frac{\pi}{4})}{10^3t+1}-\frac{\sqrt{2}}{2}\right]. \tag{47}$$

The geometry of the bi-material example as well as the manufactured solution (46) are displayed in Fig. 6. The material properties for this example are listed in Table 1.

Table 1
Material properties for the bi-material convergence example.

	ρ_0 [kg/m^3]	$\overline{E}$ [Pa]	ν [−]	μ [Pa]	κ [Pa]	$\overline{c}$ [m/s]
Domain 1	500.0	2998.0	0.499	1000.0	5.0×10^5	2.4487
Domain 2	100.0	29,980.0	0.499	1.0×10^4	5.0×10^6	17.3147

Note the different material wave propagation speeds $\overline{c}=\sqrt{\overline{E}/\rho_0}$. The components of the body force used in the numerical implementation are given by

$$\begin{aligned} f_1^* &= -10X_1(1-X_1)(1-2X_1)X_2^2(1-X_2)^2M_2(t) \\ &\quad -\frac{\partial}{\partial X_1}P_{11}(\boldsymbol{u}^*)-\frac{\partial}{\partial X_2}P_{12}(\boldsymbol{u}^*), \\ f_2^* &= 10X_1^2(1-X_1)^2X_2(1-X_2)(1-2X_2)M_2(t) \\ &\quad -\frac{\partial}{\partial X_1}P_{21}(\boldsymbol{u}^*)-\frac{\partial}{\partial X_2}P_{22}(\boldsymbol{u}^*) \end{aligned}, \tag{48}$$

where

$$\mathcal{M}_2(t) = 10^6\cdot\left[2\frac{sin(10^3t+\frac{\pi}{4})}{(10^3t+1)^3}-1\frac{sin(10^3t+\frac{\pi}{4})}{10^3t+1}-2\frac{cos(10^3t+\frac{\pi}{4})}{(10^3t+1)^2}\right]. \tag{49}$$

Fig. 7 displays the motion of the point M, (see Fig. 6(a)), computed with the midpoint, $\alpha^{1,2}=1/2$, asynchronous integrator, $\Delta t^1/\Delta t^2=1/2$. Although the spatial h and temporal Δt discretizations are mutually coupled in general, the spatial discretization often influences the vertical shift (amplitude) whereas the time discretization changes the horizontal variations (frequency) as can be observed in Fig. 7. Note that the zero motion of point M in the X_2 direction is correctly predicted.

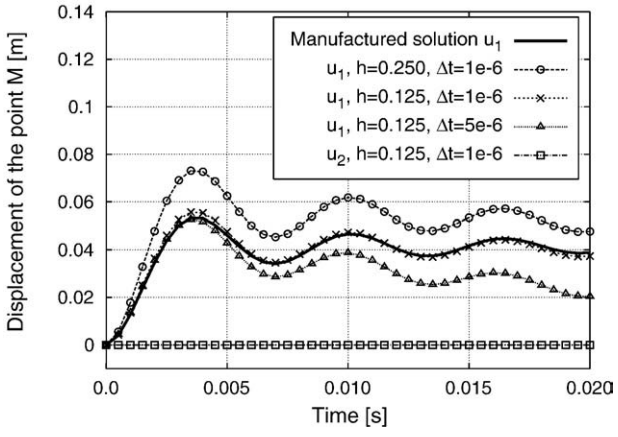

Fig. 7. Motion of point M as shown in Fig. 6. The units used are [m] for h and [s] for Δt.

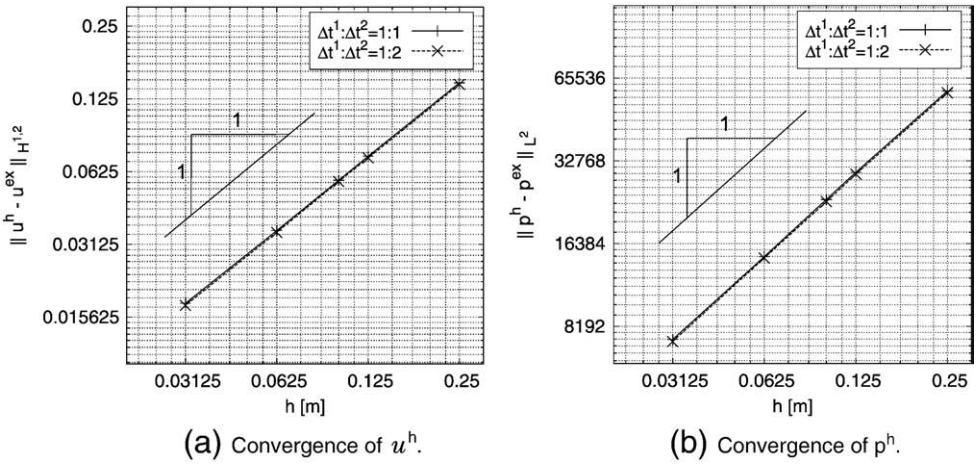

Fig. 8. Spatial convergence for bi-material test at $t = 0.004$ s.

Fig. 8 shows the spatial convergence for both the displacement $\boldsymbol{u}^h$ and pressure p^h. The $H^{1,2}$ Sobolev and L^2 norms are used for $\boldsymbol{u}^h$ and p^h, respectively. Observed in Fig. 8, the optimal convergence rates are obtained for both the displacement and the pressure in both the synchronous and asynchronous cases. Structured grids of 4×4, 8×8, 16×16, 32×32 and 64×64 elements are used to compute the convergence rates (Fig. 8).

Fig. 9 shows the temporal convergence for the bi-material test problem. Since the ratio of errors between spatial and temporal discretizations is not known, we evaluate the error as $\mathcal{E}_t = |\boldsymbol{u}^h - \boldsymbol{u}^{ex}| - |\boldsymbol{u}^h - \boldsymbol{u}^h(\Delta t \to 0)|$ to eliminate the discretization error and to allow for easy visualization. The order of the error can be interpreted as $\mathcal{E}_t = \mathcal{O}(h) + \mathcal{O}(\Delta t) - \mathcal{O}(h)$, which leaves only the time influence. The time converged solution $\boldsymbol{u}^h(\Delta t \to 0)$ is computed with Δt one thousand times smaller than the smallest evaluated time in Fig. 9. The optimal second-order convergence is obtained for both synchronous and asynchronous integrators.

Since the material is nearly-incompressible in this study, we apply an implicit integrator to solve the problem. However, the optimal convergence rates both in space and time are preserved for explicit, $\alpha = 0$, $\alpha = 1$, as well as for mixed integration schemes, $\alpha^1 = 1/2$, $\alpha^2 = 0$, and $\alpha^1 = 0$, $\alpha^2 = 1/2$ with an arbitrary sub-stepping as has been tested on a different example, since a fully explicit integrator might experience numerical difficulties as $\nu \to 1/2$.

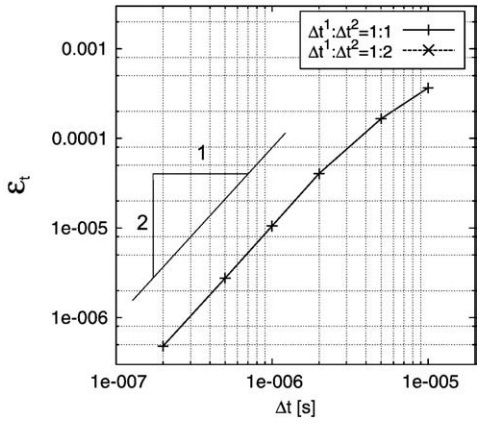

Fig. 9. Temporal convergence for a bi-material test. The error is plotted as $\mathcal{E}_t = |\boldsymbol{u}^h - \boldsymbol{u}^{ex}| - |\boldsymbol{u}^h - \boldsymbol{u}^h(\Delta t \to 0)|$ for easy visualization. Mesh composed of 10×10 elements is used in this test.

5.2. Stability study

To investigate the stability of our asynchronous integrators we again use the method of manufactured solutions. However, simple harmonic motion is now selected in order to establish the stability criteria. The domain geometry and manufactured solution are shown in Fig. 10. The manufactured solution $\boldsymbol{u}^*$ and the body force $\boldsymbol{f}^*$ are chosen as

$$
\begin{aligned}
u_1^*(X_1, X_2, t) &= X_1(1-X_1)X_2(1-X_2)\left[cos(10^3 t)-1\right],\\
u_2^*(X_1, X_2, t) &= X_1(1-X_1)X_2(1-X_2)\left[cos(10^3 t)-1\right],\\
f_1^* &= -10^6 X_1(1-X_1)X_2(1-X_2)cos\left(10^3 t\right)\\
&\quad -\frac{\partial}{\partial X_1}P_{11}\left(\boldsymbol{u}^*\right)-\frac{\partial}{\partial X_2}P_{12}\left(\boldsymbol{u}^*\right),\\
f_2^* &= -10^6 X_1(1-X_1)X_2(1-X_2)cos\left(10^3 t\right)\\
&\quad -\frac{\partial}{\partial X_1}P_{21}\left(\boldsymbol{u}^*\right)-\frac{\partial}{\partial X_2}P_{22}\left(\boldsymbol{u}^*\right).
\end{aligned}
\tag{50}
$$

In this stability study, the spatial discretization is fixed at 10×10 elements.

Fig. 11 shows the motion of point M (see Fig. 10(a)) and the energy evolution during the simulation. Note that the kinetic energy is very small in this example. Also note that due to the applied body forces, Eq. (50), our forcing term is non-conservative since $\boldsymbol{f}^* \neq 0$. Thus, the total energy in the system is negative.

Fig. 12 shows two inherent instabilities encountered in this problem. We classify these instabilities as a global instability, Fig. 12(a), and a local instability, Fig. 12(b), respectively. The error of the energy evolution for the global instability is depicted in Fig. 13(a). As one can observe, the energy becomes unbounded for larger time steps whereas the bounded energy solution, typical for the variational integrators that exactly conserve the value of a "nearby" Hamiltonian [31], is maintained for $\Delta t = 5e-5$ s. On the other hand, for the local instability, the energy grows exponentially causing the solution to rapidly diverge, which results in the collapse of the algorithm in the Newton-Raphson method (Fig. 13(b)).

We are also interested in the evolution of the angular momentum, since it is an important conserved quantity. Fig. 14 displays the error dispersion of the angular momentum for the case of global instability (Figs. 12(a) and 13(a)). Once more, the bounded solution oscillating around zero is obtained for stable integration while the large error scattering, for which the motions u_1 and u_2 become asymmetric, is observed for the unstable integration. Note that for many variational

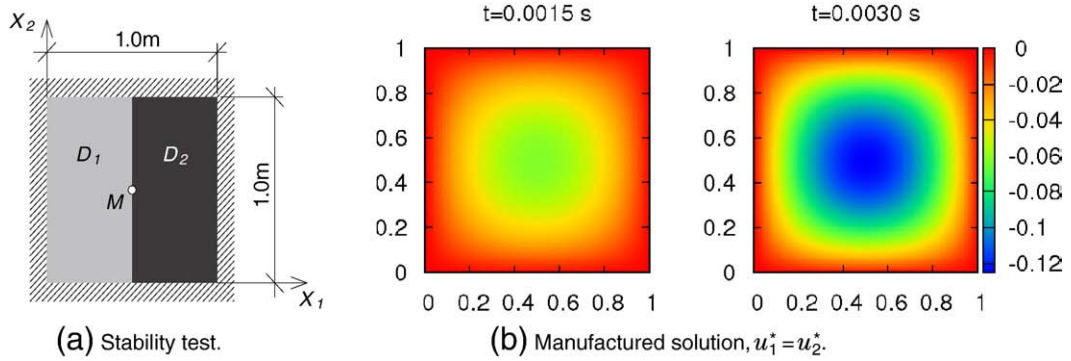

Fig. 10. Method of manufactured solutions with a harmonic motion. Material properties are as follows. Domain 1: $\overline{E} = 0.55$ GPa, $\mu = 0.25$ GPa, $\rho_0 = 1000$ kg/m^3, $\overline{c} = 741.62$ m/s; Domain 2: $\overline{E} = 2.20$ GPa, $\mu = 1.00$ GPa, $\rho_0 = 1000$ kg/m^3, $\overline{c} = 1483.24$ m/s.

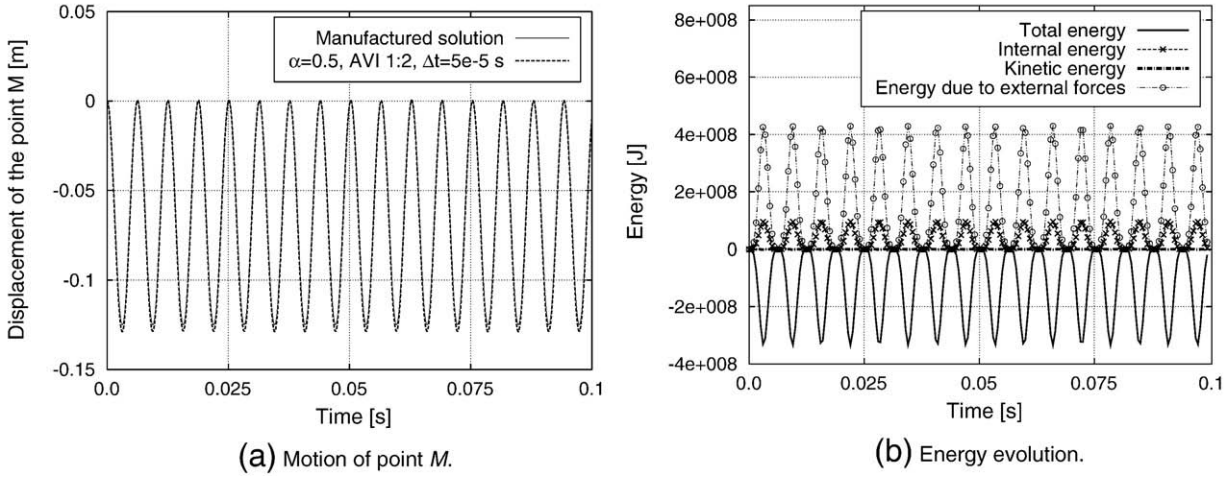

Fig. 11. Method of manufactured solutions with a harmonic motion. The asynchronous (1:2) and implicit ($\alpha^{1,2} = 1/2$) integrator is used. Note that 10,000 time steps are used to solve the reference solution.

integrators the angular momentum is preserved to within machine precision as shown in prior works [34]. However, the implicit Newmark algorithm, which is variational under a near-identity change of coordinate forces, also experiences an oscillatory behavior as presented in Fig. 14, and this oscillatory behavior will persist *indefinitely* [34]. In our case, we have not been able to identify one cause. The common interface interpolation, asynchronous time stepping and mixed $\boldsymbol{u}, p, \theta$ variational scheme are all potentially contributing to this behavior.

To understand the stability limit further, and to physically interpret the equations derived in Section 4, we compute the stability limits by

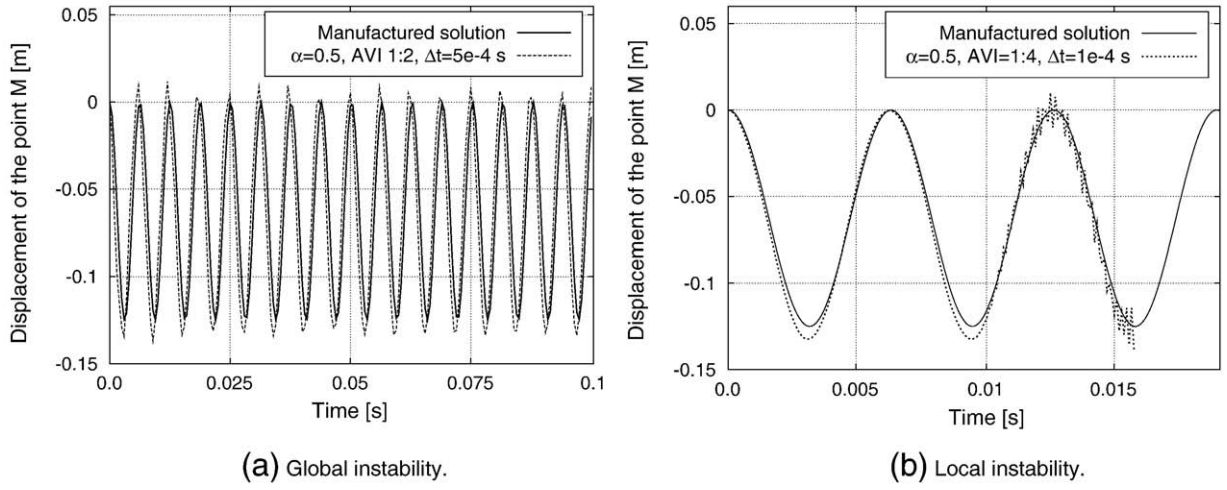

Fig. 12. Two potential types of instabilities observed for this problem.

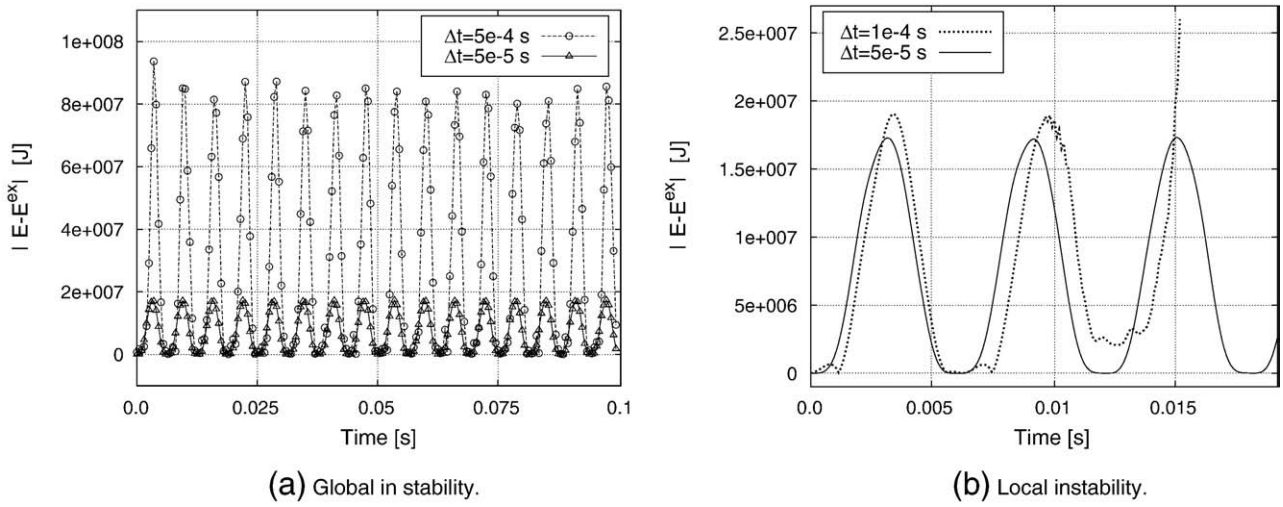

Fig. 13. The error in the energy evolution for the global and the local types of instabilities. The exact energy E^{ex} is computed from the manufactured solution (50) using Eqs. (5) and (6).

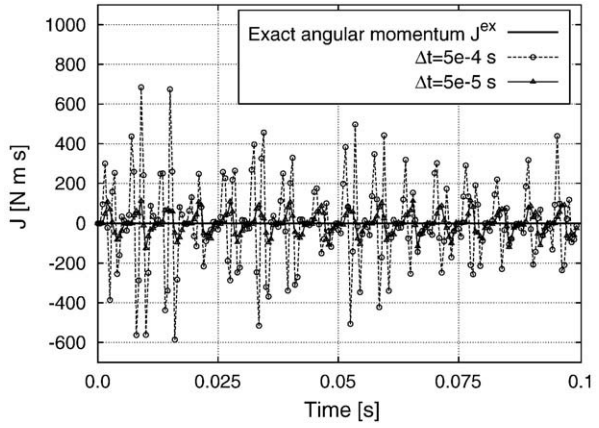

Fig. 14. The error evolution of the angular momentum. Note that $J^{ex}=0$ for this example.

varying the substep ratios on both the stiff and soft sides. We base our stability analysis on testing whether any position exceeds a bounding value or whether the nonlinear solution routine fails. The phase error represented by thin lines, in Fig. 15, is computed by comparing the average solution period $per(h,\ \Delta t)=\sum_{i=1}^{n} per_i/n$ with the reference solution period $per(\mathbf{u}^*)$. Note that Fig. 15 is very similar to that presented for the ODEs in our previous work [18].

As indicated by Eq. (C.12), the energy is preserved with $c_n\Delta t^3$ error. Conditional stability depicted for 1:1 time integration in both Fig. 15 (a) and (b) is a manifestation of this condition. Regardless of the substep ratio (1:6 or 6:1), the critical time step drops deeply when asynchronous time stepping is invoked. The local stability state bounded by Eq. (45) is likely reason for such a drop. However, the stability limit does not deteriorate further when the time interval subdivision is refined more. We contribute this behavior to a global energy balance represented by Eq. (41). Note again that Eq. (41) represents a sum of unbalanced energy projections between $_{n-1,i}$ and $_{n,i}$ substeps, where the projection surface coincides with the linear constraint interpolation (Eq. (24)).

Fig. 15(a) shows the numerically evaluated stability limit for varying substeps on the nonstiff subdomain. Due to the selected material constants, the energy error for a soft domain is smaller and less influential on coupling than its stiff domain counterpart. Thus, in this plot the stability limit is largely above the accuracy limit when changing the number of substeps on the nonstiff side. Fig. 15(b) plots the stability limit for varying substeps in the stiff region. As can be seen

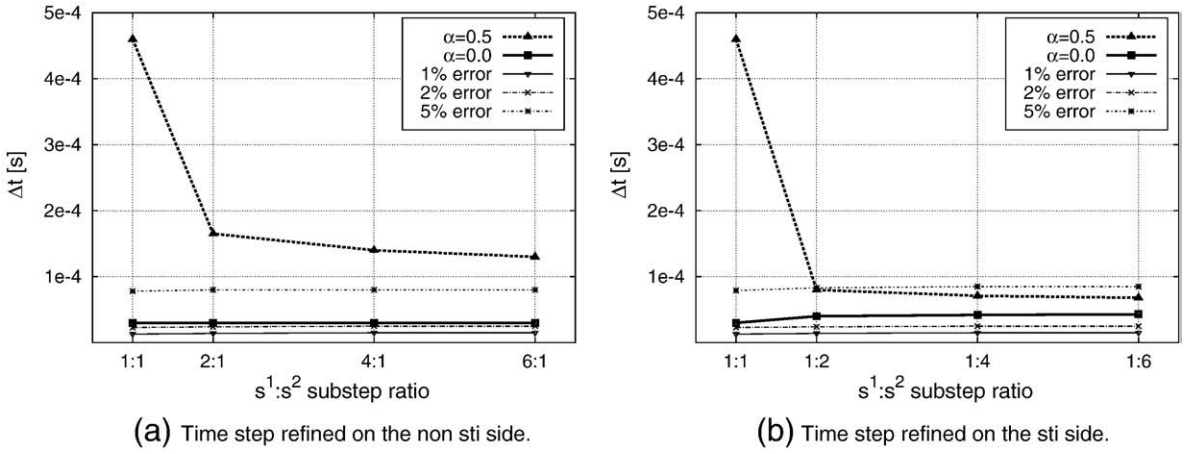

Fig. 15. Bold solid and dashed lines are stability limits. Thin lines are constant error curves showing Δt that achieved specified error. For both values of α, the time step to achieve an engineering error is in reasonable relationship to stability limits. For $\alpha=1/2$ integrator, the stability limit initially drops in changing from synchronous to asynchronous, but then becomes independent of the time step ratio. For $\alpha=0$ integrator, the stability limit increases by a factor of 1.43 from 1:1 to 6:1 ratio when the stiff side time step is refined.

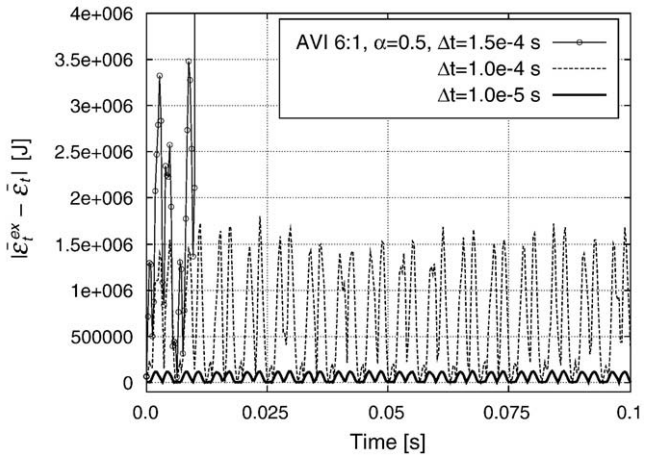

Fig. 16. The global energy error $|\bar{\mathcal{E}}_t^{ex} - \bar{\mathcal{E}}_t|$ over the system time step as predicted by Eq. (16). The exact global energy error $\bar{\mathcal{E}}_t^{ex}$ is computed from the manufactured solution (50) using Eq. (41), where $\Delta\bar{\mathcal{E}}_{n,i}^{ex} = E_{i+1/2}^{ex} - E_{i-1/2}^{ex}$ and $\Delta\bar{\mathcal{E}}_{n-1,i}^{ex} = E_{n-1,i+1/2}^{ex} - E_{n-1,i-1/2}^{ex}$.

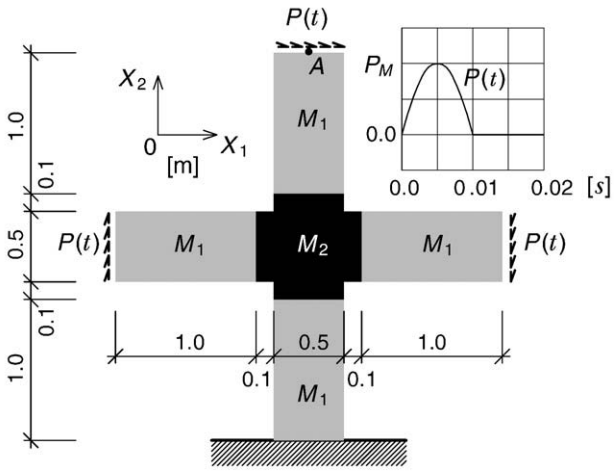

Fig. 17. Geometry, boundary conditions and loading history for the composite system. The loading impulse is prescribed as $P(t) = 1.0 \times 10^7 \sin(100.0\pi t)$. The black domain is made of a stiff and dense material, M_2, while the light grey domains are made of a more compliant and less dense material, M_1 (see Table 2). The element size $h = 0.05$ m. The total number of elements is 980.

in Fig. 15(b), the stability limit drops by factor of 5.75 by going from synchronous to asynchronous time steps for $\alpha = 1/2$ integrator. For $\alpha = 0$ integrator, the stability limit increases by factor of 1.43 from a 1:1 to 1:6 ratio, which is due to our space–time force balance (Eq. (30)). The sharper initial reduction of the stability limit, compared to the case of varying substeps in the nonstiff domain, is again attributed to the magnitude of the energy error accumulated and exchanged through the common interface from the stiff to the soft domain.

Fig. 16 shows the global energy error as predicted by Eq. (41). We select the implicit asynchronous time integrator, $\alpha^{1,2} = 1/2$, with a 6:1 ratio (The last bounding value from Fig. 15(a)). All parameters are fixed in this study, since we are investigating the effect of the time step on the error measure depicted in Fig. 16. As can be observed, for $\Delta t = 1.5\text{e}{-4}$ s the global energy error becomes wildly oscillatory, and the solution fails in the Newton-Raphson routine. For $\Delta t = 1.0\text{e}{-4}$ s, the global energy error becomes bounded and reaches the maximum value of $\sim 1.5\text{e}+6$ J (Note that we base our stability analysis on testing whether any position exceeds a bounding value not an energy, or whether the nonlinear solution routine fails). When we decrease the time step by an order from $\Delta t = 1.0\text{e}{-4}$ s to $\Delta t = 1.0\text{e}{-5}$ s, the energy error decays cubically as predicted by the global error estimate Eq. (41), and reaches the maximum value of $\sim 1.5\text{e}+3$ J.

Although we lost the $c_n \Delta t^3$ energy conservation locally in time, we gained the ability for each domain to use a different time step for the required accuracy in that domain. Moreover, the global energy error has been preserved with $\tilde{c}_n \Delta t^3$. In our tests, the stability limit for the time step still exceeded or coincided with the time step required to attain a reasonable engineering accuracy (accuracy of ~5% is achieved for the asynchronous time stepping at the stability limit). Whether this holds is of course problem-dependent. It also shows that the coupling is as important as the individual integrators used in each subdomain. It is interesting to observe that a simple estimate for the critical time step, $\Delta t_{cr} = h/\overline{c}$, provides a reasonable measure of a stability criterion for an explicit integrator. For our bi-material example, we compute the conservative estimate $\Delta t_{cr} = h/\overline{c} \approx 10^{-5}$ s (using the wave speed of the stiffer material), which is in agreement with our numerical study depicted in Fig. 15.

The long time integration is an important issue in many engineering applications as mentioned in the introduction. Note that we have investigated only a moderate number of time steps, as shown in Fig. 10. Further study is essential in assessing the long time performance of our integrators. For ODEs, we have presented the long time integration performance in [18].

5.3. Mixed integration study

For problems where the accuracy requirement in one domain would limit the system time step, asynchronous integrators allow other domains to use larger time steps. To understand the error evolution for such scenario, we investigate the composite material system made of stiff and soft components under an impulse loading. The geometry, loading history and boundary conditions are shown in Fig. 17. We use explicit, $\alpha^2 = 0$, integrator for the stiff domain and the implicit integrator, $\alpha^1 = 1/2$, for the soft regions. The material properties are listed in Table 2.

Fig. 18 shows the motion of a heterogeneous structure at three different time steps. Very large deformations can be observed for the soft domains, while a rigid like motion is spotted for the inner stiff region.

Fig. 19 depicts the motion of the point A (top arm in Fig. 17). Note that after the initial loading, the motion of the structure becomes periodic.

Examining how the time refinement affects the error, we see in Fig. 20 that refining the time step on soft domains reduces the error by 92%, whereas refining on the nonstiff side, which is prone to effect the stability (Fig. 15(b)), has little effect. In this case, the energy error in the soft arms and its transfer to the stiff middle one is the main source of the inaccuracy. This indicates that we can take larger steps on the stiff side without affecting the accuracy, and smaller steps in the compliant regions to gain the accuracy required.

This result is somewhat contrary to stability investigations (Fig. 15), where refining the nonstiff domain had a smaller effect on the critical time step. However, recall that the energy error, and thus potentially the stability, is influenced by other factors, such as material properties, the size of the subdomains, the length of the common interface, etc. In this example, we attribute this behavior to

Table 2
Material properties for the composite structure example.

	ρ_0 [kg/m^3]	$\overline{E}$ [Pa]	ν [−]	κ [Pa]	μ [Pa]	$\overline{c}$ [m/s]
M_1	1000.0	1.0×10^8	0.499	1.6667×10^{10}	3.3356×10^7	316.2278
M_2	1500.0	1.0×10^9	0.499	1.6667×10^{11}	3.3356×10^8	816.4966

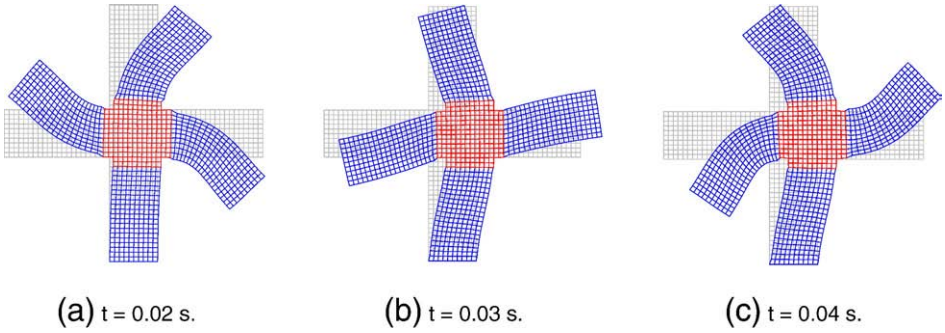

Fig. 18. Motion of the heterogeneous structure at three different time steps. The mixed integration with $\Delta t = 5e-5$ s and $s^1{:}s^2 = 2{:}1$ is used in this example.

vastly different boundary and loading conditions as well as to different sizes of the stiff/soft subdomains.

To compare the complexity of asynchronous and synchronous integrators, such as the Newmark method, we investigate the number of operations required to solve the system Eq. (31). Note that in our current implementation, we use the consistent and not lumped mass matrix. Therefore, we solve the system of algebraic equations no matter if the integrator is explicit or implicit, and thus, our analysis time is mostly governed by the time required to solve several systems of algebraic equations. We focus on both $\Delta t/\Delta t_1 = 8/1$ and $\Delta t/\Delta t_2 = 8/1$ cases. There are 3360 degrees of freedom in soft regions M_1, and 782 degrees of freedom in the stiff middle domain M_2 for $\Delta t = \Delta t_1 = \Delta t_2$. The computational cost of solving a system of algebraic equations by a sparse direct solver can be estimated in two-dimensions as $\mathcal{O}(N^{3/2})$, where N is the number of equations [23]. Since we are dealing with nonlinear problems, we usually have four to five iterations for a give time step. For a synchronous method to integrate a give time interval ($\Delta t = \Delta t_1 = \Delta t_2 = 8/8$ in this study), we can estimate the computational cost as $8\times4\times\mathcal{O}(4142^{3/2}) \approx 8.5\times10^6$. First, let us consider the case $\Delta t/\Delta t_1 = 8/1$, i.e., the soft arms are integrated with a small time step. Note that for this case the error drops by 92% when compared to a synchronous time stepping, and thus, we consider eight single steps of synchronous integrator as a good measure. Since the large domain is integrated with a small time step, the number of equations grows to $N = 27,662$ and the number of operations is given by $4\times\mathcal{O}(27662^{3/2}) \approx 18.4\times10^6$. Although we solve the large matrix, we eliminate many matrix assemblies that are quite expensive for nonlinear problems and are not accounted for in this estimate. Therefore, the synchronous method is ~2.16 times faster for this example. However, when we integrate with the small time step the stiff region M_2, only a small number of equations is added to the system and by the same estimate the asynchronous integrator is ~2.23 times faster ($4\times\mathcal{O}(9616^{3/2}) \approx 3.8\times10^6$) that the synchronous one. Unfortunately, no gain in accuracy is obtained in this case (Fig. 20). However, different applications would yield different estimates making the proposed asynchronous method sometimes more and sometimes less effective. Also, a solution strategy similar to that adopted in FETI-DP [15], as mentioned in Section 3, will improve the efficiency.

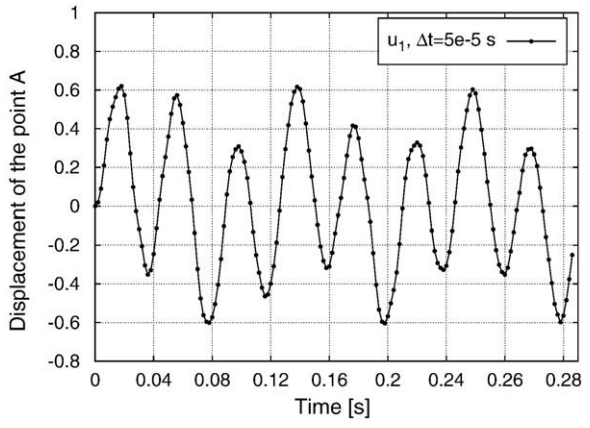

Fig. 19. The u_1 motion of the point A in Fig. 17. The mixed integration with $\Delta t = 5e-5$ s and $s^1{:}s^2 = 2{:}1$ is used in this example.

To indicate optimal rates of convergence of the Newton-Raphson scheme, the residuals Eq. (28) for the displacement $\mathbf{u}^h$, pressure p^h and residuals Eq. (30) for the common interface motion $\mathbf{w}^h$ after each Newton-Raphson iteration are listed in Table 3. Note that since the constraint Eq. (15) is linear, the residuals Eq. (29) for Lagrange multipliers $\mathscr{R}_\lambda$ attain machine precision values immediately after the first iteration, as do residuals Eq. (30) for the common interface motion $\mathbf{w}^h$ (see Table 3), and are therefore not listed in Table 3. Also, note that for the simple dilatational strain energy density $U(\theta)$ Eq. (7), the residuals for the volume unknown $\mathscr{R}_\theta$ attain machine precision values immediately after the first iteration and are therefore not listed in Table 3 as well.

6. Conclusions

In this paper, we have proposed asynchronous multi-domain variational integrators for nonlinear hyperelastic solids. Variational time integration schemes have been derived in the context of the Lagrangian variational framework, and the three-field de Veubeke-

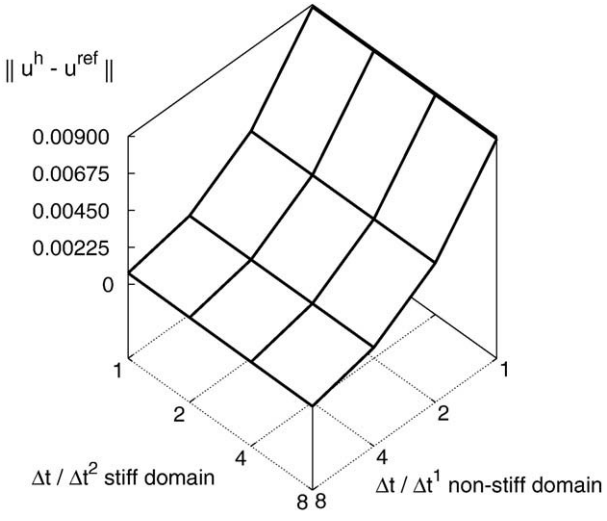

Fig. 20. The change of the error as time steps for stiff domain and nonstiff domains are refined, with fixed system time step $\Delta t = 1e-4$ s. As the time step is refined on the compliant domain, along the left axis, error is reduced by 92% compared to 1:1 integrator. As the time step is refined on the stiff domain, along the right axis, there is little change in error. The reference solution $\boldsymbol{u}^{ref}$ is obtained using synchronous explicit integrator $\alpha^{1,2} = 0$ with $\Delta t = 5e-7$ s. The L^2 norm is computed for the time interval [0, 0.1] s.

Table 3
Residuals after each Newton-Raphson iteration of the nonlinear solution step for the composite structure in Fig. 17. Residuals are evaluated at time $t = 0.035$ s and the similar convergence properties are observed throughout the whole transient analysis.

Iteration number	$\|\mathscr{R}_u\|$	$\|\mathscr{R}_p\|$	$\|\mathscr{R}_w\|$
1	4.877303e+03	4.693986e−02	2.982091e−01
2	4.193527e−01	1.920041e−02	3.748244e−14
3	3.876491e−04	4.017160e−05	1.199953e−14
4	4.601880e−07	4.010048e−08	1.831532e−14
5	2.013276e−12	1.871391e−13	7.249979e−15

Hu-Washizu variational principle has been used for the spatial discretization to accommodate the incompressibility constraint. The subdomain coupling has been achieved by the Lagrange multiplier method to ensure the continuity of the displacement field at the interface between subdomains. In particular, the dual domain decomposition method has been exploited in order to preserve the efficient parallelization of the algorithm.

The Energy method has been employed to assess the energy conservation of the proposed midpoint asynchronous integrator. The local and the global energy conservation criteria have been derived. For synchronous time integration, we retain the $\mathcal{O}(\Delta t^3)$ energy evolution while asynchronous time stepping is locally bounded by the $\mathcal{O}((\Delta t^k)^2)$ estimate. The global energy balance across the interface between domains still holds with $\mathcal{O}(\Delta t^3)$. Based on the numerical observations, the investigated integrators are conditionally stable only. However, we have not investigated the nonlinear stability of our integrators and their observed conditional stability in detail, and more rigorous study is required.

Several examples have been solved to show the consistency and robustness of the method. We have adopted the method of manufactured solutions to show the optimal convergence rates as well as to investigate the energy evolution and the stability criteria. The mixed time integration, implicit versus explicit, has been presented in order to illustrate the solution error control, and the applicability of the method in engineering applications. Only moderate time asynchronicity has been investigated in this work, $\sim \Delta t_1/\Delta t_2 = 1/8$; future investigation is necessary to extend this approach to large time step differences. Moreover, a moderate number of time steps has been studied (~10,000), and further study is required to assess the long time performance of our integrators.

The emphasis of this work has been on the development of asynchronous multi-domain time integrators and their energy conservation. However, real-size applications are likely to necessitate solution strategy improvements, when a system of algebraic equations is solved, requiring an efficient parallel implementation of the computational scheme presented above. The extension to three-dimensions is also of importance. Ultimately, we want to extend the proposed method to examples with non-matching discretizations and multi-physics problems.

Acknowledgments

The authors gratefully acknowledge support from the Center for Simulation of Advanced Rockets (CSAR) under contract number B523819 the U.S. Department of Energy as a part of its Advanced Simulation and Computing program (ASC). The authors also thank Prof. Joseph M. Powers from University of Notre Dame for numerous suggestions that improved the presentation of this paper.

Appendix A. Constraint on displacements or velocities

Here, we compare the constraint on displacements to that on velocities. First, let us consider a split single degree of freedom oscillator with two domains constrained to a common interface by displacement constraint using local Lagrange multipliers λ^a and λ^b, as shown in Fig. A.1.

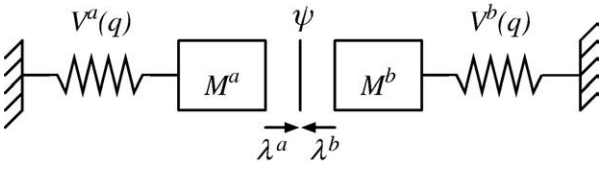

Fig. A.1. Split single degree-of-freedom system with masses constrained together.

For this scenario, the augmented discrete Lagrangian yields

$$\hat{L}_d = L_d^a(q_n^a, q_{n+1}^a) + L_d^b\left(q_n^b, q_{n+1}^b\right) + (q_{n+1}^a - \psi_{n+1})\boldsymbol{\lambda}_{n+1}^a + \left(q_{n+1}^b - \psi_{n+1}\right)\boldsymbol{\lambda}_{n+1}^b, \tag{A.1}$$

where L_d^a and L_d^b are the discrete Lagrangians for each subdomain. With the augmented action sum, $\hat{A}_d = \sum_{n=0}^{N-1} \hat{L}_d \approx \int_{t_0}^{t_N} \hat{L}(q, \dot{q})\mathrm{d}t$, where N is the number of time steps, the discrete Euler-Lagrange equations associated with the interface yield

$$\frac{\partial \hat{A}_d}{\lambda_{n+1}^a} = q_{n+1}^a - \psi_{n+1} = 0, \tag{A.2}$$

$$\frac{\partial \hat{A}_d}{\lambda_{n+1}^b} = q_{n+1}^b - \psi_{n+1} = 0, \tag{A.3}$$

$$\frac{\partial \hat{A}_d}{\psi_n} = \lambda_n^a + \lambda_n^b = 0. \tag{A.4}$$

The physical interpretation of the Lagrange multipliers for the displacement constraint is well known, with $\lambda \left[\frac{\text{kg m}}{S^2}\right]$ representing an interface force.

Next, let us consider a constraint on velocities with discrete Lagrangian given by

$$\hat{L}_d = L_d^a(q_n^a, q_{n+1}^a) + L_d^b(q_n^b, q_{n+1}^b) + \left(\frac{q_{n+1}^a - q_n^a}{\Delta t} - \frac{\psi_{n+1} - \psi_n}{\Delta t}\right)\tilde{\lambda}_{n+1}^a + \left(\frac{q_{n+1}^b - q_n^b}{\Delta t} - \frac{\psi_{n+1} - \psi_n}{\Delta t}\right)\tilde{\lambda}_{n+1}^b. \tag{A.5}$$

Here, we have used a simple discrete derivative as in Eq. (21). As in the case of displacement constraint, $\hat{A}_d = \sum_{n=0}^{N-1} \hat{L}_d$, and the discrete Euler-Lagrange equations associated with the interface read

$$\frac{\partial \hat{A}_d}{\tilde{\lambda}_{n+1}^a} = (q_{n+1}^a - \psi_{n+1}) + \underbrace{(\psi_n - q_n^a)}_{=0,\ \text{from I.C.}} = 0, \tag{A.6}$$

$$\frac{\partial \hat{A}_d}{\tilde{\lambda}_{n+1}^b} = \left(q_{n+1}^b - \psi_{n+1}\right) + \underbrace{\left(\psi_n - q_n^b\right)}_{=0,\ \text{from I.C.}} = 0, \tag{A.7}$$

$$\frac{\partial \hat{A}_d}{\psi_n} = \left(\tilde{\lambda}_{n+1}^a - \tilde{\lambda}_n^a\right) + \left(\tilde{\lambda}_{n+1}^b - \tilde{\lambda}_n^b\right) = \Delta\tilde{\lambda}_n^a + \Delta\tilde{\lambda}_n^b = 0. \tag{A.8}$$

Assuming that there are no discontinuities at rest, $n=0$, we can eliminate the second term in Eqs. (A.6) and (A.7) by applying the initial conditions (I.C.). Thus, the Euler-Lagrange equations associated with the Lagrange multipliers are identical to those from the displacement constraint. Simple substitution of variables renders Eqs. (A.4) and (A.8) identical also. Finally, let us present the physical interpretation for the Lagrange multipliers, $\tilde{\lambda}$, and Eq. (A.8). Since Eq. (A.5) represents the work $\left[\frac{\text{kg m}^2}{S^2}\right]$ and the constraint the velocity $\left[\frac{\text{m}}{S}\right]$, the Lagrange multipliers $\tilde{\lambda}$ denote the generalized interface momentum $\left[\frac{\text{kg m}}{S}\right]$. Thus, Eq. (A.8) states that the change in the discrete momentum rate across the interface is constant (note that Δt was canceled in Eq. (A.8)).

Appendix B. Consistent linearization

Here, we give individual linearized contributions of K^i and L^i, respectively. The matrices K^i read

$$\begin{aligned}
\delta\boldsymbol{u}^h \cdot K_{uu}^i\left[\Delta\boldsymbol{u}_{i+1}^h\right] &= D\mathscr{R}_{\boldsymbol{u}}\left[\Delta\boldsymbol{u}_{i+1}^h\right] = -\frac{1}{\Delta t^k}\int_{\Omega_0^k}\rho_0\Delta\boldsymbol{u}_{i+1}^h\cdot\delta\boldsymbol{u}^h d\Omega_0^k + \Delta t^k\Big\{-\alpha(1-\alpha)\int_{\Omega_0^k}\left[\boldsymbol{F}_{i+\alpha}^T\left(\nabla_0\delta\boldsymbol{u}^h\right)\right] : \mathscr{S}_{i+\alpha} : \left[\left(\nabla_0\left(\Delta\boldsymbol{u}_{i+1}^h\right)\right)\right]d\Omega_0^k \\
&\quad -\alpha(1-\alpha)\int_{\Omega_0^k}\left[\left(\nabla_0\delta\boldsymbol{u}^h\right)^T\nabla_0\left(\Delta\boldsymbol{u}_{i+1}^h\right)\right] : \hat{\boldsymbol{S}}'_{i+\alpha}d\Omega_0^k \quad -\alpha(1-\alpha)\int_{\Omega_0^k}p_{i+\alpha}^h J_{i+\alpha}\left[tr\left(\boldsymbol{F}_{i+\alpha}^{-1}\nabla_0\left(\Delta\boldsymbol{u}_{i+1}^h\right)\right)tr\left(\boldsymbol{F}_{i+\alpha}^{-1}\nabla_0\delta\boldsymbol{u}^h\right)\right]d\Omega_0^k \\
&\quad +\alpha(1-\alpha)\int_{\Omega_0^k}p_{i+\alpha}^h J_{i+\alpha}\left[tr\left(\boldsymbol{F}_{i+\alpha}^{-1}\nabla_0\left(\Delta\boldsymbol{u}_{i+1}^h\right)\boldsymbol{F}_{i+\alpha}^{-1}\nabla_0\delta\boldsymbol{u}^h\right)\right]d\Omega_0^k\Big\}, \\
\delta\theta^h \cdot K_{\theta\theta}^i\left[\Delta\theta_{i+1}^h\right] &= D\mathscr{R}_{\theta}\left[\Delta\theta_{i+1}^h\right] = -\alpha(1-\alpha)\Delta t^k\int_{\Omega_0^k}\kappa\left[\Delta\theta_{i+1}^h\right]\delta\theta^h d\Omega_0^k, \\
\delta p^h \cdot K_{pu}^i\left[\Delta\boldsymbol{u}_{i+1}^h\right] &= D\mathscr{R}_p\left[\Delta\boldsymbol{u}_{i+1}^h\right] = -\alpha(1-\alpha)\Delta t^k\int_{\Omega_0^k}\left(\delta p^h\right)J_{i+\alpha}C_{i+\alpha}^{-1} : \left[\boldsymbol{F}_{i+\alpha}^T\left(\nabla_0\left(\Delta\boldsymbol{u}_{i+1}^h\right)\right)\right]d\Omega_0^k, \\
\delta p^h \cdot K_{p\theta}^i\left[\Delta\theta_{i+1}^h\right] &= D\mathscr{R}_p\left[\Delta\theta_{i+1}^h\right] = \alpha(1-\alpha)\Delta t^k\int_{\Omega_0^k}\left(\delta p^h\right)\left[\Delta\theta_{i+1}^h\right]d\Omega_0^k,
\end{aligned} \tag{B.1}$$

where

$$\mathscr{S}_{i+\alpha} = 4\frac{\partial^2\widehat{\boldsymbol{W}}}{\partial\boldsymbol{C}\partial\boldsymbol{C}}(\boldsymbol{C}_{i+\alpha}). \tag{B.2}$$

The matrices L^i read

$$\begin{aligned}
\delta\boldsymbol{u}^h \cdot \boldsymbol{L}_{uu}^i\left[\Delta\boldsymbol{u}_i^h\right] &= D\mathscr{R}_{\boldsymbol{u}}\left[\Delta\boldsymbol{u}_i^h\right] = \frac{2}{\Delta t^k}\int_{\Omega_0^k}\rho_0\Delta\boldsymbol{u}^h\cdot\delta\boldsymbol{u}^h d\Omega_0^k + \Delta t^k\Big\{-\alpha^2\int_{\Omega_0^k}\left[\boldsymbol{F}_{i-1+\alpha}^T\left(\nabla_0\delta\boldsymbol{u}^h\right)\right] : \mathscr{S}_{i-1+\alpha} : \left[\left(\nabla_0\left(\Delta\boldsymbol{u}_i^h\right)\right)\right]d\Omega_0^k \\
&\quad -\alpha^2\int_{\Omega_0^k}\left[\left(\nabla_0\delta\boldsymbol{u}^h\right)^T\nabla_0\left(\Delta\boldsymbol{u}_i^h\right)\right] : \hat{\boldsymbol{S}}'_{i-1+\alpha}d\Omega_0^k - \alpha^2\int_{\Omega_0^k}p_{i-1+\alpha}^h J_{i-1+\alpha}\left[\mathrm{tr}\left(\boldsymbol{F}_{i-1+\alpha}^{-1}\nabla_0\left(\Delta\boldsymbol{u}_i^h\right)\right)\mathrm{tr}\left(\boldsymbol{F}_{i-1+\alpha}^{-1}\nabla_0\delta\boldsymbol{u}^h\right)\right]d\Omega_0^k \\
&\quad +\alpha^2\int_{\Omega_0^k}p_{i-1+\alpha}^h J_{i-1+\alpha}\left[\mathrm{tr}\left(\boldsymbol{F}_{i-1+\alpha}^{-1}\nabla_0\left(\Delta\boldsymbol{u}_i^h\right)\boldsymbol{F}_{i-1+\alpha}^{-1}\nabla_0\delta\boldsymbol{u}^h\right)\right]d\Omega_0^k - (1-\alpha)^2\int_{\Omega_0^k}\left[\boldsymbol{F}_{i+\alpha}^T\left(\nabla_0\delta\boldsymbol{u}^h\right)\right] : \mathscr{S}_{i+\alpha} : \left[\left(\nabla_0\left(\Delta\boldsymbol{u}_i^h\right)\right)\right]d\Omega_0^k \\
&\quad -(1-\alpha)^2\int_{\Omega_0^k}\left[\left(\nabla_0\delta\boldsymbol{u}^h\right)^T\nabla_0\left(\Delta\boldsymbol{u}_i^h\right)\right] : \hat{\boldsymbol{S}}'_{i+\alpha}d\Omega_0^k - (1-\alpha)^2\int_{\Omega_0^k}p_{i+\alpha}^h J_{i+\alpha}\left[\mathrm{tr}\left(\boldsymbol{F}_{i+\alpha}^{-1}\nabla_0\left(\Delta\boldsymbol{u}_i^h\right)\right)\mathrm{tr}\left(\boldsymbol{F}_{i+\alpha}^{-1}\nabla_0\delta\boldsymbol{u}^h\right)\right]d\Omega_0^k \\
&\quad +(1-\alpha)^2\int_{\Omega_0^k}p_{i+\alpha}^h J_{i+\alpha}\left[\mathrm{tr}\left(\boldsymbol{F}_{i+\alpha}^{-1}\nabla_0\left(\Delta\boldsymbol{u}_i^h\right)\boldsymbol{F}_{i+\alpha}^{-1}\nabla_0\delta\boldsymbol{u}^h\right)\right]d\Omega_0^k\Big\}, \\
\delta\theta^h\cdot\mathrm{L}_{\theta\theta}^i\left[\Delta\theta_i^h\right] &= D\mathscr{R}_{\theta}\left[\Delta\theta_i^h\right] = -\left(\alpha^2+(1-\alpha)^2\right)\Delta t^k\int_{\Omega_0^k}\kappa\left[\Delta\theta_i^h\right]\delta\theta^h d\Omega_0^k, \\
\delta p^h\cdot\boldsymbol{L}_{pu}^i\left[\Delta\boldsymbol{u}_i^h\right] &= D\mathscr{R}_p\left[\Delta\boldsymbol{u}_i^h\right] = -\alpha^2\Delta t^k\int_{\Omega_0^k}\left(\delta p^h\right)J_{i-1+\alpha}\mathrm{C}_{i-1+\alpha}^{-1} : \left[\boldsymbol{F}_{i-1+\alpha}^T\left(\nabla_0\left(\Delta\boldsymbol{u}_i^h\right)\right)\right]d\Omega_0^k - (1-\alpha)^2\Delta t^k\int_{\Omega_0^k}\left(\delta p^h\right)J_{i+\alpha}\mathrm{C}_{i+\alpha}^{-1} : \left[\boldsymbol{F}_{i+\alpha}^T\left(\nabla_0\left(\Delta\boldsymbol{u}_i^h\right)\right)\right]d\Omega_0^k, \\
\delta p^h\cdot\boldsymbol{L}_{p\theta}^i\left[\Delta\theta_i^h\right] &= D\mathscr{R}_p\left[\Delta\theta_i^h\right] = \left(\alpha^2+(1-\alpha)^2\right)\Delta t^k\int_{\Omega_0^k}\left(\delta p^h\right)\left[\Delta\theta_i^h\right]d\Omega_0^k,
\end{aligned} \tag{B.3}$$

where

$$\mathscr{D}_{i-1+\alpha} = 4\,\frac{\partial^2 \widehat{\boldsymbol{W}}}{\partial \mathrm{C}\partial \mathrm{C}}\left(\mathrm{C}_{i-1+\alpha}\right). \tag{B.4}$$

Note that $\forall i = 3,\ldots,\ s^k\,\mathrm{N}^i = \mathrm{K}^{i-1}$.

The coupling matrices are given by

$$\begin{aligned}
\delta\boldsymbol{\lambda}^h\cdot \mathrm{C}_{\lambda u}\left[\Delta \boldsymbol{u}^h_{i+1}\right] &= D_{\cdot}\mathscr{R}_{\boldsymbol{\lambda}}\left[\Delta \boldsymbol{u}^h_{i+1}\right] = \Delta t^k \int_{\Gamma^k}\left(\mathrm{B}^k\left(\Delta \boldsymbol{u}^h_{i+1}\right)\right)^T \delta\boldsymbol{\lambda}^h \mathrm{d}S_0,\\
\delta\boldsymbol{\lambda}^h\cdot \mathrm{C}_{\lambda w}\left[\Delta \boldsymbol{w}^h_{n+1}\right] &= D_{\cdot}\mathscr{R}_{\boldsymbol{\lambda}}\left[\Delta \boldsymbol{w}^h_{n+1}\right] = -\Delta t^k \int_{\Gamma^k}\left(\mathrm{D}^k\left(\Delta \boldsymbol{w}^h_{n+1}\right)\right)^T \delta\boldsymbol{\lambda}^h \mathrm{d}S_0.
\end{aligned} \tag{B.5}$$

Appendix C. Energy error estimate

Here, we derive the Energy error estimate Eq. (41). First, let us recall the discrete residual equation $\mathscr{R}_{\mathrm{u}}$, Eq. 28(a), given by

$$\begin{aligned}
0 = &-\int_{\Omega_0^k}\rho_0\left(\frac{\boldsymbol{u}^h_{i+1}-2\boldsymbol{u}^h_i+\boldsymbol{u}^h_{i-1}}{\Delta t^k}\right)\cdot\delta\boldsymbol{u}^h \mathrm{d}\Omega_0^k - \frac{1}{2}\Delta t^k\int_{\Omega_0^k}\left(\frac{\partial \widehat{\boldsymbol{W}}}{\partial \boldsymbol{F}}\left(\boldsymbol{F}_{i-\frac{1}{2}}\right) + p^h_{i-\frac{1}{2}}J_{i-\frac{1}{2}}\boldsymbol{F}^{-T}_{i-\frac{1}{2}}\right) : \left(\nabla_0\delta\mathrm{u}^h\right)\mathrm{d}\Omega_0^k\\
&-\frac{1}{2}\Delta t^k\int_{\Omega_0^k}\left(\frac{\partial \widehat{\boldsymbol{W}}}{\partial \boldsymbol{F}}\left(\boldsymbol{F}_{i+\frac{1}{2}}\right) + p^h_{i+\frac{1}{2}}J_{i+\frac{1}{2}}\boldsymbol{F}^{-T}_{i+\frac{1}{2}}\right) : \left(\nabla_0\delta\boldsymbol{u}^h\right)\mathrm{d}\Omega_0^k + \Delta t^k\int_{\Gamma^k}\left(\mathrm{B}^k\left(\delta\boldsymbol{u}^h\right)\right)^T\left(\boldsymbol{\lambda}^h_i\right)^k \mathrm{d}S_0.
\end{aligned} \tag{C.1}$$

Next, we take $\delta\mathrm{u}^h = (\phi^h_{i+1} - \phi_{i-1}{}^h)/(2\Delta t^k)$ in Eq. (C.1) and write

$$\begin{aligned}
0 = &-\frac{1}{2}\int_{\Omega_0^k}\rho_0\left(\frac{\boldsymbol{u}^h_{i+1}-\boldsymbol{u}^h_i}{\Delta t^k}\right)\cdot\left(\frac{\boldsymbol{u}^h_{i+1}-\boldsymbol{u}^h_i}{\Delta t^k}\right)\mathrm{d}\Omega_0^k + \frac{1}{2}\int_{\Omega_0^k}\rho_0\left(\frac{\boldsymbol{u}^h_i-\boldsymbol{u}^h_{i-1}}{\Delta t^k}\right)\cdot\left(\frac{\boldsymbol{u}^h_i-\boldsymbol{u}^h_{i-1}}{\Delta t^k}\right)\mathrm{d}\Omega_0^k - \frac{1}{2}\int_{\Omega_0^k}\left(\frac{\partial \widehat{\boldsymbol{W}}}{\partial \boldsymbol{F}}\left(\boldsymbol{F}_{i-\frac{1}{2}}\right) + p^h_{i-\frac{1}{2}}J_{i-\frac{1}{2}}\boldsymbol{F}^{-T}_{i-\frac{1}{2}}\right) : \left(\boldsymbol{F}_{i+\frac{1}{2}}-\boldsymbol{F}_{i-\frac{1}{2}}\right)\mathrm{d}\Omega_0^k\\
&-\frac{1}{2}\int_{\Omega_0^k}\left(\frac{\partial \widehat{\boldsymbol{W}}}{\partial \boldsymbol{F}}\left(\boldsymbol{F}_{i+\frac{1}{2}}\right) + p^h_{i+\frac{1}{2}}J_{i+\frac{1}{2}}\boldsymbol{F}^{-T}_{i+\frac{1}{2}}\right) : \left(\boldsymbol{F}_{i+\frac{1}{2}}-\boldsymbol{F}_{i-\frac{1}{2}}\right)\mathrm{d}\Omega_0^k + \frac{1}{2}\int_{\Gamma^k}\left(\mathrm{B}^k\left(\phi^h_{i+1}-\phi^h_{i-1}\right)\right)^T\left(\boldsymbol{\lambda}^h_i\right)^k \mathrm{d}S_0.
\end{aligned} \tag{C.2}$$

Taking advantage of a standard Taylor expansion, we collect individual terms of the deviatoric energy function (Eq. (7)) as well as of the pressure geometric term, which yields

$$\begin{aligned}
0 = &-\left(T^k_{i+\frac{1}{2}}-T^k_{i-\frac{1}{2}}\right) - \int_{\Omega_0^k}\left(\widehat{\boldsymbol{W}}_{i+\frac{1}{2}}-\widehat{\boldsymbol{W}}_{i-\frac{1}{2}}\right)\mathrm{d}\Omega_0^k - \int_{\Omega_0^k}\left(p^h_{i+\frac{1}{2}}J_{i+\frac{1}{2}}-p^h_{i-\frac{1}{2}}J_{i-\frac{1}{2}}\right)\mathrm{d}\Omega_0^k + \frac{1}{2}\int_{\Omega_0^k}\left(J_{i+\frac{1}{2}}+J_{i-\frac{1}{2}}\right)\left(p^h_{i+\frac{1}{2}}-p^h_{i-\frac{1}{2}}\right)\mathrm{d}\Omega_0^k\\
&+\frac{1}{2}\int_{\Gamma^k}\left(\mathrm{B}^k\left(\phi^h_{i+1}-\phi^h_{i-1}\right)\right)^T\left(\boldsymbol{\lambda}^h_i\right)^k \mathrm{d}S_0 + c_i\left(\Delta t^k\right)^3,
\end{aligned} \tag{C.3}$$

where T^k denotes the discrete kinetic energy, Eqs. (5) and (22) (the first term), expressed using the simple midpoint rule, Eq. (21). As in Hauret and Le Tallec [22], we will say that c_i depends on the approximate solution at times i and $i+1$, respectively. In general, the constants c_i are dependent on material properties, size of the subdomains, length of the common interface for subdomain ^{k}, etc. The Taylor expansion of the potential function $\hat{W}(\mathrm{F})$, the pressure geometric contribution pJ and the volumetric function $U(\theta)$ are given for clarity in Appendix D.

Similarly, we substitute $\left(p^h_{i+\frac{1}{2}}-p^h_{i-\frac{1}{2}}\right)$ for δp^h in the discrete residual $\mathcal{R}_p$, Eq. (28)(c), and obtain

$$0 = -\frac{1}{2}\int_{\Omega_0^k}\left(J_{i+\frac{1}{2}}+J_{i-\frac{1}{2}}\right)\left(p^h_{i+\frac{1}{2}}-p^h_{i-\frac{1}{2}}\right)\mathrm{d}\Omega_0^k + \frac{1}{2}\int_{\Omega_0^k}\left(\theta^h_{i-\frac{1}{2}}+\theta^h_{i+\frac{1}{2}}\right)\left(p^h_{i+\frac{1}{2}}-p^h_{i-\frac{1}{2}}\right)\mathrm{d}\Omega_0^k. \tag{C.4}$$

After substituting Eq. (C.4) into Eq. (C.3) and using

$$\frac{1}{2}\left(\theta^h_{i+\frac{1}{2}}+\theta^h_{i-\frac{1}{2}}\right)\left(p^h_{i+\frac{1}{2}}-p^h_{i-\frac{1}{2}}\right) = -\frac{1}{2}\left(p^h_{i+\frac{1}{2}}+p^h_{i-\frac{1}{2}}\right)\left(\theta^h_{i+\frac{1}{2}}-\theta^h_{i-\frac{1}{2}}\right) + p^h_{i+\frac{1}{2}}\theta^h_{i+\frac{1}{2}} - p^h_{i-\frac{1}{2}}\theta^h_{i-\frac{1}{2}},$$

we get

$$0 = -\left(T^k_{i+\frac{1}{2}} - T^k_{i-\frac{1}{2}}\right) - \int_{\Omega^k_0}\left(\widehat{\boldsymbol{W}}_{i+\frac{1}{2}} - \widehat{\boldsymbol{W}}_{i-\frac{1}{2}}\right)\mathrm{d}\Omega^k_0 - \int_{\Omega^k_0}\left(p^h_{i+\frac{1}{2}}\left(J_{i+\frac{1}{2}} - \theta^h_{i+\frac{1}{2}}\right) - p^h_{i-\frac{1}{2}}\left(J_{i-\frac{1}{2}} - \theta^h_{i-\frac{1}{2}}\right)\right)\mathrm{d}\Omega^k_0$$
$$-\frac{1}{2}\int_{\Omega^k_0}\left(p^h_{i+\frac{1}{2}} + p^h_{i-\frac{1}{2}}\right)\left(\theta^h_{i+\frac{1}{2}} - \theta^h_{i-\frac{1}{2}}\right)\mathrm{d}\Omega^k_0 + \frac{1}{2}\int_{\Gamma^k}\left(\mathrm{B}^k\left(\phi^h_{i+1} - \phi^h_{i-1}\right)\right)^T\left(\boldsymbol{\lambda}^h_i\right)^k\mathrm{d}S_0 + c_i\left(\Delta t^k\right)^3. \tag{C.5}$$

Finally, in the last residual equation $\mathscr{R}_\theta$, Eq. (28), we exchange $\delta\theta^h$ with $\left(\theta^h_{i+\frac{1}{2}} - \theta^h_{i-\frac{1}{2}}\right)/\Delta t^k$:

$$0 = -\frac{\kappa}{2}\int_{\Omega^k_0}\left[\left(\theta^h_{i+\frac{1}{2}} - 1\right) + \left(\theta^h_{i-\frac{1}{2}} - 1\right)\right]\left(\theta^h_{i+\frac{1}{2}} - \theta^h_{i-\frac{1}{2}}\right)\mathrm{d}\Omega^k_0 + \frac{1}{2}\int_{\Omega^k_0}\left[p^h_{i+\frac{1}{2}} + p^h_{i-\frac{1}{2}}\right]\left(\theta^h_{i+\frac{1}{2}} - \theta^h_{i-\frac{1}{2}}\right)\mathrm{d}\Omega^k_0. \tag{C.6}$$

We again substitute Eq. (C.6) to Eq. (C.5) and use the Taylor expansion of the volumetric function, $U(\theta)$, to reduce Eq. (C.5) after substitution of Eq. (C.6) to

$$\left(T^k_{i+\frac{1}{2}} + V^k_{i+\frac{1}{2}}\right) - \left(T^k_{i-\frac{1}{2}} + V^k_{i-\frac{1}{2}}\right) = \frac{1}{2}\int_{\Gamma^k}\left(\mathrm{B}^k\left(\phi^h_{i+1} - \phi^h_{i-1}\right)\right)^T\left(\boldsymbol{\lambda}^h_i\right)^k\mathrm{d}S_0 + c_i\left(\Delta t^k\right)^3. \tag{C.7}$$

The final energetic contribution that needs to be added is the discrete energy flowing through the interface due to the domain decomposition method, (the last term in Eq. (22)). Since we use the variational method for constraint enforcement, Eq. (14), the energy flux through the interface is naturally balanced by the residual equation $\mathscr{R}_\lambda$, Eq. (29), that gives

$$I^k_i = \int_{\Gamma^k}\Phi^k\left(\mathrm{u}^h_i, \boldsymbol{w}^h_i\right)^T\left(\boldsymbol{\lambda}^h\right)^k_i\mathrm{d}S_0 = \int_{\Gamma^k}\left(\mathrm{B}^k\left(\mathrm{u}^h_i\right) - \mathrm{D}^k\left(\boldsymbol{w}^h_i\right)\right)^T\left(\boldsymbol{\lambda}^h\right)^k_{n-1,i}\mathrm{d}S_0 = 0, \quad \forall i, \tag{C.8}$$

where $(\lambda^h)^k_{n-1,i} = (\lambda^h)^k(t_{n-1} + i\Delta t^k)$.

The total energy evolution from the time step $_{i-1/2}$ to $_{i+1/2}$ can now be written as

$$E^k_{i+\frac{1}{2}} - E^k_{i-\frac{1}{2}} = \left(T^k_{i+\frac{1}{2}} + V^k_{i+\frac{1}{2}} + I^k_{i+\frac{1}{2}}\right) - \left(T^k_{i-\frac{1}{2}} + V^k_{i-\frac{1}{2}} + I^k_{i-\frac{1}{2}}\right) = \frac{1}{2}\int_{\Gamma^k}\left(\mathrm{B}^k\left(\phi^h_{i+1} - \phi^h_{i-1}\right)\right)^T\left(\boldsymbol{\lambda}^h_i\right)^k\mathrm{d}S_0 + c_i\left(\Delta t^k\right)^3. \tag{C.9}$$

Note that for the synchronous time stepping, the integral over the interfaces

$$\sum_{k=1}^{N_D}\frac{1}{2}\int_{\Gamma^k}\left(\mathrm{B}^k\left(\phi^h_{n+1} - \phi^h_{n-1}\right)\right)^T\left(\boldsymbol{\lambda}^h\right)^k_n\mathrm{d}S_0 = 0. \tag{C.10}$$

The consequence of this balance is the local force equilibrium, Eq. (30) (Lagrange multipliers are of the same magnitude and an opposite sign as shown in Fig. 5(a)), that reads

$$-\sum_{k=1}^{N_D}\Delta t^k\int_{\Gamma^r}\mathrm{D}^k\left(\delta\boldsymbol{w}^h\right)^T\left(\boldsymbol{\lambda}^h\right)^k_n\mathrm{d}S_0 = 0, \quad \text{which holds} \quad \forall n. \tag{C.11}$$

Here, we have used the constraint Eq. (15) to go from Eqs. (C.11)–(C.10). Thus, the energy evolution yields

$$E^k_{n+\frac{1}{2}} - E^k_{n-\frac{1}{2}} = c_n\Delta t^3. \tag{C.12}$$

Note again that c_n only depends on the approximate solution at times n and $n+1$ [22].

To investigate the energy evolution for the asynchronous time integrators, we rewrite Eq. (C.9) in the incremental form

$$\Delta\mathscr{E}^k_{n,i} = \frac{1}{2}\int_{\Gamma^k}\mathrm{D}^k\left(\boldsymbol{w}^h_{n,i+1} - \boldsymbol{w}^h_{n,i-1}\right)^T\left(\boldsymbol{\lambda}^h\right)^k_{n,i}\mathrm{d}S_0 + c_i\left(\Delta t^k\right)^3. \tag{C.13}$$

Here, we used the constraint function, Eq. (15), to replace the sub-domain displacements, $\mathbf{u}^h$, with their counterparts on the common interface $\mathbf{w}^h$. Expanding Eq. (C.13) by recursion formula, we get

$$\Delta\mathscr{E}^k_{n,i} = \frac{1}{s^k}\int_{\Gamma^k} \mathrm{D}^k(\boldsymbol{w}_{n+1}-\boldsymbol{w}_n)^T\left(\boldsymbol{\lambda}^h\right)^k_{n,i}\mathrm{d}S_0 + c_i\left(\Delta t^k\right)^3,\ \Delta\mathscr{E}^k_{n-1,i} = \frac{1}{s^k}\int_{\Gamma^k} \mathrm{D}^k(\boldsymbol{w}_n-\boldsymbol{w}_{n-1})^T\left(\boldsymbol{\lambda}^h\right)^k_{n-1,i}\mathrm{d}S_0 + c_i\left(\Delta t^k\right)^3, \tag{C.14}$$

with $\mathbf{w}_{n,i+1}-\mathbf{w}_{n,i-1}=2/s^k(\mathbf{w}_{n+1}-\mathbf{w}_n)$, and similarly for $_{n-1,i}$ time step, which is a consequence of our linear interpolation of the common interface (Eq. (24)). Now we employ Taylor expansion for the common interface motion as we did for the potential energy functions and write

$$\Delta\mathcal{E}^k_{n,i} = \frac{1}{s^k}\int_{\Gamma^k} \mathrm{D}^k\left(\dot{\boldsymbol{w}}_n\Delta t + \frac{1}{2}\ddot{\boldsymbol{w}}_n\Delta t^2 + c_n\Delta t^3\right)^T(\boldsymbol{\lambda}^h)^k_{n,i}\mathrm{d}S_0 + c_i(\Delta t^k)^3, \Delta\mathcal{E}^k_{n-1,i} = \frac{1}{s^k}\int_{\Gamma^k} \mathrm{D}^k\left(\dot{\boldsymbol{w}}_n\Delta t - \frac{1}{2}\ddot{\boldsymbol{w}}_n\Delta t^2 + c_n\Delta t^3\right)^T(\boldsymbol{\lambda}^h)^k_{n-1,i}\mathrm{d}S_0 + c_i(\Delta t^k)^3. \tag{C.15}$$

Multiplying Eq. (C.15) by $(1-i/s^k)$ and Eq. (15) by (i/s^k), and summing the equations together, we arrive at

$$\begin{aligned} 0 = \sum_{k=1}^{N_D}\sum_{i=0}^{s^k-1}\Bigg[&\left(\frac{i}{s^k}\right)\Delta\mathcal{E}^k_{n-1,i} + \left(1-\frac{i}{s^k}\right)\Delta\mathcal{E}^k_{n,i} - \frac{1}{s^k}\int_{\Gamma^k}\boldsymbol{D}^k\left(\dot{\boldsymbol{w}}_n\Delta t + c_n\Delta t^3\right)\left(\left(\frac{i}{s^k}\right)(\boldsymbol{\lambda}^h)^k_{n-1,i} + \left(1-\frac{i}{s^k}\right)(\boldsymbol{\lambda}^h)^k_{n,i}\right)\mathrm{d}S_0 \\ &-\frac{1}{s^k}\int_{\Gamma^k}\Delta t^2\mathrm{D}^k\left(\frac{1}{2}\ddot{\boldsymbol{w}}_n\right)\left(\left(1-\frac{i}{s^k}\right)(\boldsymbol{\lambda}^h)^k_{n,i} - \left(\frac{i}{s^k}\right)(\boldsymbol{\lambda}^h)^k_{n-1,i}\right)\mathrm{d}S_0 - c_i\left(\Delta t^k\right)^3\Bigg]. \end{aligned} \tag{C.16}$$

Note that D^k is a linear Boolean operator (Eq. (15)). Since we are interested in estimating the order, we approximate the third line in Eq. (C.16) without loss of generality with

$$\begin{aligned} &-\frac{1}{s^k}\int_{\Gamma^k}\Delta t^2\mathrm{D}^k\left(\frac{1}{2}\ddot{\boldsymbol{w}}_n\right)\left(\left(1-\frac{i}{s^k}\right)(\boldsymbol{\lambda}^h)^k_{n,i} - \left(\frac{i}{s^k}\right)(\boldsymbol{\lambda}^h)^k_{n-1,i}\right)\mathrm{d}S_0 \approx -\frac{1}{s^k}\int_{\Gamma^k}\Delta t^3\mathrm{D}^k\left(\frac{1}{2}\ddot{\boldsymbol{w}}_n\right)\left(c^*\frac{(\boldsymbol{\lambda}^h)^k_{n,i}-(\boldsymbol{\lambda}^h)^k_{n-1,i}}{\Delta t}\right)\mathrm{d}S_0 = \\ &-\frac{1}{s^k}\int_{\Gamma^k}\Delta t^3\mathrm{D}^k\left(\frac{1}{2}\ddot{\boldsymbol{w}}_n\right)\left(c^*(\dot{\boldsymbol{\lambda}}^h)^k_{n,i} + c_n\Delta t\right)\mathrm{d}S_0, \end{aligned} \tag{C.17}$$

where c^* does not depend on Δt. Taking into consideration the last residual equation $\mathcal{R}_w$, Eq. (30), which makes the second line in Eq. (C.16) zero, and arbitrariness of $\delta\mathbf{w}^h$, we reduce Eq. (C.16) using Eq. (C.17) to

$$\overline{\mathcal{E}}_t = \sum_{k=1}^{N_D}\sum_{i=0}^{s^k-1}\left(\frac{i}{s^k}\right)\Delta\mathcal{E}^k_{n-1,i} + \left(1-\frac{i}{s^k}\right)\Delta\mathcal{E}^k_{n,i} = \tilde{c}_n\Delta t^3, \tag{C.18}$$

where $\tilde{c}_n = \max\{c^*, c_n\}$.

Appendix D. Taylor expansion of constitutive equations

Here, we describe the Taylor expansion used in the conservation analysis. For the deviatoric part of the potential function we get

$$\begin{aligned} \widehat{W}_{i+\alpha} - \widehat{W}_{i-1+\alpha} &= \frac{1}{2}\left(\frac{\partial\widehat{W}}{\partial\boldsymbol{F}}(\boldsymbol{F}_{i-1+\alpha}) + \frac{\partial\widehat{W}}{\partial\boldsymbol{F}}(\boldsymbol{F}_{i+\alpha})\right) : (\boldsymbol{F}_{i+\alpha}-\boldsymbol{F}_{i-1+\alpha}) + c\frac{\partial^3\widehat{W}}{\partial\boldsymbol{F}^3}(\boldsymbol{F}^*)(\boldsymbol{F}_{i+\alpha}-\boldsymbol{F}_{i-1+\alpha})^3 \\ &= \frac{1}{2}\left(\frac{\partial\widehat{W}}{\partial\boldsymbol{F}}(\boldsymbol{F}_{i-1+\alpha}) + \frac{\partial\widehat{W}}{\partial\boldsymbol{F}}(\boldsymbol{F}_{i+\alpha})\right) : (\boldsymbol{F}_{i+\alpha}-\boldsymbol{F}_{i-1+\alpha}) + \frac{c_i}{8}\left(\Delta t^k\right)^3\frac{\partial^3\widehat{W}}{\partial\boldsymbol{F}^3}(\boldsymbol{F}^*)\left(\dot{\boldsymbol{F}}_{i+\alpha} + \dot{\boldsymbol{F}}_{i-1+\alpha}\right)^3, \end{aligned} \tag{D.1}$$

with an unknown matrix F^*.

The volumetric strain density potential can be expanded as

$$U\left(\theta^h_{i+\alpha}\right) - U\left(\theta^h_{i-1+\alpha}\right) = \frac{1}{2}\left(\frac{\partial U}{\partial\theta^h}\left(\theta^h_{i-1+\alpha}\right) + \frac{\partial U}{\partial\theta^h}\left(\theta^h_{i+\alpha}\right)\right) : \left(\theta^h_{i+\alpha}-\theta^h_{i-1+\alpha}\right) + c_i\left(\Delta t^k\right)^3. \tag{D.2}$$

Finally, the pressure volumetric contribution can be given by

$$\begin{aligned} p^h_{i+\alpha}J_{i+\alpha} - p^h_{i-1+\alpha}J_{i-1+\alpha} = &\frac{1}{2}\left(J(\mathrm{C}_{i+\alpha}) + J(\mathrm{C}_{i-1+\alpha})\right)\cdot\left(p^h_{i+\alpha}-p^h_{i-1+\alpha}\right) + \frac{1}{2}\left(p^h_{i+\alpha}J_{i+\alpha}\boldsymbol{F}^{-T}_{i+\alpha} + p^h_{i-1+\alpha}J_{i-1+\alpha}\boldsymbol{F}^{-T}_{i-1+\alpha}\right) : \\ &(\boldsymbol{F}_{i+\alpha}-\boldsymbol{F}_{i-1+\alpha}) + c_i\left(\Delta t^k\right)^3. \end{aligned} \tag{D.3}$$

References

[1] R. Abedi, R.B. Haber, B. Petracovici, A spacetime discontinuous galerkin method for elastodynamics with element-level balance of linear momentum, Computer Methods in Applied Mechanics and Engineering 195 (2006) 3247–3273.
[2] F. Armero, Energy-dissipative momentum-conserving time-stepping algorithms for finite strain multiplicative plasticity, Computer Methods in Applied Mechanics and Engineering 195 (2006) 4862–4889.
[3] F. Armero, I. Romero, On the formulation of high-frequency dissipative time-stepping algorithms for nonlinear dynamics. part ii. second-order methods, Computer Methods in Applied Mechanics and Engineering 190 (2001) 6783–6824.
[4] S.N. Atluri, E. Reissner, On the formulation of variational theorems involving volume constraints, Computational Mechanics 5 (1989) 337–344.
[5] T. Belytschko, Partitioned and adaptive algorithms for explicit time integration, in: W. Wunderlich, E. Stein, K.J. Bathe (Eds.), Nonlinear Finite Element Analysis in Structural Mechanics, Springer, 1981, pp. 572–584.
[6] T. Belytschko, R. Mullen, Stability of explicit–implicit mesh partitions in time integration, International Journal for Numerical Methods in Engineering 12 (1978) 1575–1586.
[7] T. Belytschko, R. Mullen, Mesh partitions of explicit–implicit time integration, in: K. Bathe, J. Oden, W. Wunderlich (Eds.), Formulations and Computational Algorithms in Finite Element Analysis, MIT Press, 1991, pp. 673–690.
[8] T. Belytschko, H. Yen, R. Mullen, Mixed methods for time integration, Computer Methods in Applied Mechanics and Engineering 17/18 (1979) 259–275.
[9] F. Brezzi, L. Marini, The three-field formulation for elasticity problems, GAMM Mitteilungen 28 (2005) 124–153.
[10] A. Combescure, A. Gravouil, A numerical scheme to couple subdomains with different time-steps for predominantly linear transient analysis, Computer Methods in Applied Mechanics and Engineering 191 (2002) 1129–1157.
[11] W.J.T. Daniel, A study of the stability of subcycling algorithms in structural dynamics, Computer Methods in Applied Mechanics and Engineering 156 (1998) 1–13.
[12] J.W. Demmel, S.C. Eisenstat, J.R. Gilbert, X.S. Li, J.W.H. Liu, A supernodal approach to sparse partial pivoting, SIAM Journal on Matrix Analysis and Applications 20 (3) (1999) 720–755.
[13] D.G. Ebin, Global solutions of the equations of elastodynamics of incompressible neo-hookean materials, Proceedings of the National Academy of Sciences USA 90 (1993) 3802–3805.
[14] C. Farhat, P. Chen, J. Mandel, A scalable Lagrange multiplier based domain decomposition method for implicit time-dependent problems, International Journal for Numerical Methods in Engineering 38 (1995) 3831–3858.
[15] C. Farhat, M. Lesoinne, P. LeTallec, K. Pierson, D. Rixen, Feti-dp: a dual–primal unified feti method — part I: A faster alternative to the two-level feti method, International Journal for Numerical Methods in Engineering 50 (2001) 1523–1544.
[16] C. Farhat, F.X. Roux, A method of finite element tearing and interconnecting and its parallel solution algorithm, International Journal for Numerical Methods in Engineering 32 (1991) 1205–1227.
[17] W. Fong, E. Darve, A. Lew, Stability of asynchronous variational integrators, Journal of Computational Physics 227 (18) (2008) 8367–8394.
[18] M. Gates, K. Matouš, M.T. Heath, Asynchronous multi-domain variational integrators for non-linear problems, International Journal for Numerical Methods in Engineering 76 (2008) 1353–1378.
[19] O. Gonzalez, Exact energy and momentum conserving algorithms for general models in nonlinear elasticity, Computer Methods in Applied Mechanics and Engineering 190 (2000) 1763–1783.
[20] O. Gonzalez, J.C. Simo, On the stability of symplectic and energy–momentum algorithms for non-linear hamiltonian systems with symmetry, Computer Methods in Applied Mechanics and Engineering 134 (1996) 197–222.
[21] A. Gravouil, A. Combescure, Multi-time-step explicit–implicit method for non-linear structural dynamics, International Journal for Numerical Methods in Engineering 50 (2001) 199–225.
[22] P. Hauret, P. Le Tallec, Energy-controlling time integration methods for nonlinear elastodynamics and low-velocity impact, Computer Methods in Applied Mechanics and Engineering 195 (2006) 4890–4916.
[23] M.T. Heath, Scientific Computing: An Introductory Survey. 2nd ed, McGraw-Hill, 2002.
[24] T.J.R. Hughes, The Finite Element Method: Linear Static and Dynamic Finite Element Analysis, Prentice Hall, 1987.
[25] T.J.R. Hughes, T. Kato, J.E. Marsden, Well-posed quasi-linear second-order hyperbolic systems with applications to nonlinear elastodynamics and general relativity, Archive for Rational Mechanics and Analysis 63 (3) (1977) 273–291.
[26] T.J.R. Hughes, W. Liu, Implicit–explicit finite elements in transient analysis: Implementation and numerical examples, Journal of Applied Mechanics 45 (1978) 375–378.
[27] T.J.R. Hughes, W. Liu, Implicit–explicit finite elements in transient analysis: Stability theory, Journal of Applied Mechanics 45 (1978) 371–374.
[28] K.G. Kale, A.J. Lew, Parallel asynchronous variational integrators, International Journal for Numerical Methods in Engineering 70 (2007) 291–321.
[29] C. Kane, J.E. Marsden, M. Ortiz, M. West, Variational integrators and the Newmark algorithm for conservative and dissipative mechanical systems, International Journal for Numerical Methods in Engineering 49 (2000) 1295–1325.
[30] A. Lew, J.E. Marsden, M. Ortiz, M. West, Asynchronous variational integrators, Archive for Rational Mechanics and Analysis 167 (2003) 85–146.
[31] J.E. Marsden, M. West, Discrete mechanics and variational integrators, Acta Numerica 10 (2001) 357–514.
[32] K. Matouš, A.M. Maniatty, Finite element formulation for modeling large deformations in elasto-viscoplastic polycrystals, International Journal for Numerical Methods in Engineering 60 (2004) 2313–2333.
[33] M.O. Neal, T. Belytschko, Explicit–explicit subcycling with non-integer time step ratios for structural dynamic systems, Computer Methods in Applied Mechanics and Engineering 31 (1989) 871–880.
[34] N.M. Newmark, A method of computation for structural dynamics, Journal of the Engineering Mechanics Division 85 (1959) 67–94.
[35] M. Ortiz, A note on energy conservation and stability of nonlinear time-stepping algorithms, Computers and Structures 24 (1) (1986) 167–168.
[36] K.C. Park, C.A. Felippa, U. Gumaste, A localized version of the method of Lagrange multipliers and its applications, Computational Mechanics 24 (2000) 476–490.
[37] K.C. Park, C.A. Felippa, G. Rebel, A simple algorithm for localized construction of non-matching structural interfaces, International Journal for Numerical Methods in Engineering 53 (2002) 2117–2142.
[38] A. Prakash, K.D. Hjelmstad, A feti-based multi-time-step coupling method for newmark schemes in structural dynamics, International Journal for Numerical Methods in Engineering 61 (2004) 2183–2204.
[39] J.C. Simo, R.L. Taylor, K.S. Pister, Variational and projection methods for the volume constraint in finite deformation elasto-plasticity, Computer Methods in Applied Mechanics and Engineering 51 (1985) 177–208.
[40] P. Smolinski, S. Sleith, Explicit multi-time step methods for structural dynamics, New Methods in Transient Analysis, ASME, 1992, pp. 1–4, PVP-Vol. 246 / AMD-Vol. 143.
[41] P. Smolinski, S. Sleith, T. Belytschko, Stability of an explicit multi-time step integration algorithm for linear structural dynamics equations, Computational Mechanics 18 (1996) 236–244.
[42] A.P. Veselov, Integrable discrete-time systems and difference operators, Functional Analysis and Its Applications 22 (1988) 83–93.
[43] J.M. Wendlandt, J.E. Marsden, Mechanics integrators derived from a discrete variational principle, Physica D 106 (1997) 223–246.